

CHALMERS



Prediction of Vibrational Amplitude in Composite Sandwich Structures

Prediction and Implementation of the Orthotropic Damping in
Carbon-Fibre-Reinforced Epoxy

Master's thesis in Applied Mechanics

SIMON RYDBERG

Department of Applied Mechanics

Division of Solid Mechanics

CHALMERS UNIVERSITY OF TECHNOLOGY

Gothenburg, Sweden 2013

Master's thesis 2013:72

MASTER'S THESIS IN APPLIED MECHANICS

Prediction of Vibrational Amplitude in Composite Sandwich Structures

Prediction and Implementation of the Orthotropic Damping in
Carbon-Fibre-Reinforced Epoxy

SIMON RYDBERG

Department of Applied Mechanics
Division of Solid Mechanics
CHALMERS UNIVERSITY OF TECHNOLOGY
Gothenburg, Sweden 2013

Prediction of Vibrational Amplitude in Composite Sandwich Structures
Prediction and Implementation of the Orthotropic Damping in
Carbon-Fibre-Reinforced Epoxy
SIMON RYDBERG

© SIMON RYDBERG, 2013

Master's thesis 2013:72
ISSN 1652-8557
Department of Applied Mechanics
Division of Solid Mechanics
Chalmers University of Technology
SE-412 96 Gothenburg
Sweden
Telephone: +46 (0)31-772 1000

Chalmers Reproservice
Gothenburg, Sweden 2013

Prediction of Vibrational Amplitude in Composite Sandwich Structures
Prediction and Implementation of the Orthotropic Damping in
Carbon-Fibre-Reinforced Epoxy
Master's thesis in Applied Mechanics
SIMON RYDBERG
Department of Applied Mechanics
Division of Solid Mechanics
Chalmers University of Technology

ABSTRACT

When performing High-Cycle Fatigue (HCF) estimations of a structure, accurately defined damping is a necessity. The actual damping in a structure is often unknown and is therefore only roughly estimated. Conventional metals have low material damping which can often be neglected. Carbon-Fibre-Reinforced Epoxy (CFRE) composites on the other hand exhibit significant material damping which in addition also is orthotropic. In the present thesis a method is developed to predict the orthotropic material damping of a CFRE as well as implementing this damping in a Finite Element Analysis (FEA).

Using the Halpin-Tsai micromechanical model together with the elastic-viscoelastic correspondence principle, the homogenised orthotropic damping is predicted from experimentally determined constituent material data. The predicted damping is successfully implemented in an FEA using separate elements for stiffness and damping. The developed method is validated against results found in literature, confirming that it is possible to accurately predict the damping of different composites by tweaking the four damping parameters in the model, η_m , η_{E_1} , η_{E_2} and $\eta_{G_{12}}$.

To experimentally validate the predicted damping, a CFRE/foam sandwich beam was designed which damping for the first three bending modes was determined through ping tests. The results from the experimental testing indicate an underestimation in the numerical damping using the proposed method of approximately 20%. This underestimation is believed to mainly originate from the simplified micromechanical model used which neglects effects as e.g., fibre-matrix interface. Further underestimation is believed to be caused by neglected macromechanical effects as e.g., interlaminar stresses, which cannot be described by the First-order Shear Deformation Theory (FSDT) used in the FEA.

The results show that the composite has a large contribution to the overall damping in the sandwich structure and that it is important to accurately model the composite damping when performing dynamic analyses.

Keywords: Composite, Orthotropic damping, Experimental testing, Finite Element Analysis

SAMMANFATTNING

När en struktur analyseras för högcykelutmattning (HCF) är en korrekt bestämd dämpning en nödvändighet. Den faktiska dämpningen i en struktur är sällan känd och uppskattas därför i de flesta fall. Vanliga metaller har låg dämpning som ofta är försumbar. Kolfiber/epoxi (CFRE) komposit har i motsats betydande dämpning som dessutom är ortotrop. I detta arbete är en metod framtagen för att prediktera dämpningen i en CFRE komposit och implementeringen av denna i en FE-analys.

Genom att använda den mikromekaniska modellen Halpin-Tsai tillsammans med den elastiska-viskoelastiska principen predikteras den homogeniserade ortotropa dämpningen hos kompositen från kända egenskaper för dess beståndsdelar. Den predikterade dämpningen implementeras i en FE-analys genom att använda separata element för styvhet och dämpning. Den framtagna metoden valideras mot litterära resultat vilket visar att det är möjligt att prediktera dämpningen i kompositerna genom justering av de fyra dämpningsparametrarna, η_m , η_{E_1} , η_{E_2} and $\eta_{G_{12}}$.

För att experimentellt validera den predikterade dämpningen gjordes ping test på en CFRE/skum sandwichbalk. Resultaten från testningen visade på en underskattning i den predikterade dämpningen på ungefär 20%. Denna underskattning tros främst bero på brister i den förenklade mikromekaniska modellen som bortser från effekter som t.ex. fiber-matris-gränsskiktet. Ytterligare underskattning tros komma från bortsedda makromekaniska effekter som t.ex. interlaminära spänningar som inte kan beskrivas av första ordningens skjuvteori (FSDT) som använts i FE-analyserna.

Resultaten visar att kompositen har ett betydande bidrag till den totala dämpningen i sandwichstrukturen och att det därför är viktigt att kunna modellera dämpningen i kompositen noggrant vid dynamiska analyser.

PREFACE

This thesis has been conducted as the final part in the Master of Science degree in Applied Mechanics at Chalmers University of Technology. The work was carried out at GKN Aerospace Engine Systems in Trollhättan, Sweden during the spring and summer of 2013. The work has been supervised by Daniel Borovic and Dr. Niklas Jansson at GKN and Ass. Prof. Martin Fagerström at Chalmers. Examiner was Prof. Ragnar Larsson.

I would like to thank my supervisors and my examiner for the possibility to do this thesis and for their invaluable help and guidance throughout the project. I also wish to thank Jens Juul and Anders Lindblom at GKN and Erik Olsson at ACAB for their help in making the experimental testing possible.

Finally I would like to thank the co-workers at GKN and Chalmers for contributing to a great working environment.

Trollhättan, October 2013
Simon Rydberg

ABBREVIATIONS

ACAB	Applied Composites AB
AFC	Aft Fan Case
CFRE	Carbon-Fibre-Reinforced Epoxy
CLT	Classical Laminate Theory
DMTA	Dynamic Mechanical Thermal Analysis
DOF	Degree Of Freedom
FE	Finite Element
FEA	Finite Element Analysis
FF	Fan Frame
FFT	Fast Fourier Transform
FHF	Fan Hub Frame
FRF	Frequency Response Function
FSDT	First-order Shear Deformation Theory
GAES	GKN Aerospace Engine Systems
HCF	High-Cycle Fatigue
HSDT	Higher-order Shear Deformation Theory
IP	In-Plane
IROM	Inverse Rule Of Mixtures
OGV	Outlet Guide Vane
PMI	Polymethacrylimide
ROM	Rule Of Mixtures
RST&D	Resonance Search Track & Dwell
RTM	Resin Transfer Moulding
RVE	Representative Volume Element
SDC	Specific Damping Capacity
SDOF	Single Degree Of Freedom
SNR	Signal-to-Noise Ratio
VITAL	EnVIronmenTALly Friendly Aero Engine

CONTENTS

Abstract	i
Sammanfattning	ii
Preface	iii
Abbreviations	v
Contents	vii
1 Introduction	1
1.1 Background	1
1.2 Aim	2
1.3 Purpose	2
1.4 Limitations	3
1.5 Scope of work	3
2 Damping - prediction & implementation	5
2.1 Basic concepts in damping	5
2.1.1 Experimental damping characterisation	6
2.1.2 Measures of damping	7
2.2 Composite damping	8
2.2.1 Damping mechanisms in composites	8
2.2.2 Dynamic Mechanical Thermal Analysis of neat resin	9
2.2.3 Prediction of composite damping	12
2.2.4 FE implementation	14
2.2.5 Method summary	16
2.2.6 Validation of method against literature results	17
2.3 Foam core damping	20
3 Experimental testing	21
3.1 Test design	21
3.1.1 Specimen design	21
3.1.2 Fixture design	29
3.2 Manufacturing	31
3.3 Test execution	33
3.3.1 Ping test	33
3.3.2 HCF test	35
4 FE damping results	39
4.1 Modal analysis	39
4.2 Damping analysis	41
4.3 Correlation between FE damping and experimental results	43
5 Conclusions	45
6 Future work	47
References	48
A Manufacturing specification of sandwich beam specimen	I
B Exploded view of fixture assembly	III
C Modal analysis of fixture	V
D Matlab code	VII

1 Introduction

1.1 Background

GKN Aerospace Engine Systems (GAES) in Trollhättan, formerly Volvo Aero Corporation (VAC), develops and manufactures components for commercial and military aircraft engines together with the major engine manufacturers in the world. GKN has continuously worked with the development of lightweight components to mitigate the pollution from aircraft engines. In this process, one component identified for further development was the Outlet Guide Vane (OGV) which is the part of the Fan Frame (FF) structure connecting the Fan Hub Frame (FHF) to the Aft Fan Case (AFC). The OGV, as part of the GEnx engine can be seen in Figure 1. The OGV has the structural function of preventing deformation of the fan case and transferring loads from the main engine bearing to the wing mount. In addition to this it also has the aerodynamic function of redirecting the swirling bypass flow after the fan to axial flow.

Besides requirements on the OGV such as strength and impact properties, the vane will experience excitations from surrounding structures and bypass flow with high frequencies and many cycles during its service life. These vibrations result in a high risk of High-Cycle Fatigue (HCF). Resonance can be avoided by changing the stiffness or mass of the structure or by isolating it from the excitation source. When none of these actions are possible due to other demands on the structure, the only remaining solution is to add damping. The OGVs in current aircraft engines are made out of either hollow titanium or sandwich aluminium. These conventional metallic materials have low internal damping and the main dissipation of energy is through structural joints. Carbon-fibre-reinforced epoxy (CFRE) composites on the other hand have both high specific stiffness and high damping which makes them suitable for lightweight structures.



Figure 1: *GEnx engine with position of OGV indicated.*

As a part of a lightweight strategy in the European project, EnVironmenTALly friendly Aero Engine (VITAL), VAC developed an OGV made out of CFRE. The new generations of turbofan engines have a larger bypass structure to increase efficiency which means that the OGVs become longer. To meet the requirements of low weight it was necessary to design the OGV as a sandwich structure. In the current GKN concept the vanes are manufactured through a Resin Transfer Moulding (RTM) process and have CFRE skin and a foam core.

Due to earlier experiences, concerns have been raised about the HCF properties of the foam core. One hypothesis is that the low HCF performance of the core is due to heating of the material during the progression of the test. In an earlier thesis [19], the material heating and the following temperature rise from material damping was successfully predicted for the core material.

1.2 Aim

This thesis aims at extending the performed work in [19] towards simulation methods to predict the vibrational amplitude of the sandwich structure depending on excitation amplitude and frequency. Specifically, a method will be developed to predict the homogenised orthotropic damping properties of the composite from known constituent material data. The method will also cover the implementation of this predicted damping in a Finite Element Analysis (FEA). The accuracy of the proposed method will be evaluated using results from literature as well as experimental testing.

The following research questions will be answered in the thesis:

- What are the orthotropic damping properties of the CFRE material system in the OGV, and are they affecting the response of the sandwich structure?
- How can the orthotropic damping be modelled accurately and methodically in ANSYS® to predict the vibrational amplitude?

1.3 Purpose

The necessary steps when performing an HCF estimation of a structure can be seen in Figure 2. The purpose of the modal analysis is to identify eigenfrequencies and eigenmodes of the structure. Margins against resonances from surrounding structures and fluids are then evaluated using e.g., Campbell diagrams. The aerospace industry uses a conservative approach where no component eigenfrequency is allowed to coincide within $\pm 15\%$ of the five first engine orders at neither idle, cruise nor redline speed (maximum engine speed) to avoid resonance. Since the OGVs are heavily affected by the bypass flow the first fan blade passing frequency should also be avoided. Any identified critical eigenfrequencies at or near resonance are evaluated using a harmonic analysis to determine the response levels of the structure. Post processing of the results can then be used to evaluate the risk of HCF. To be able to perform this type of analysis the geometry, stiffness, mass and damping of the structure need to be defined as well as the exciting loads. It is the uncertainty of especially the exciting load and the damping that affect the accuracy of the HCF estimation the most. With the developed method for prediction and implementation of the composite damping covered in this thesis it will be possible to make more accurate HCF estimations of composite structures. With the ever increasing demand for lightweight and sustainable products, accurate damping prediction is a necessity.

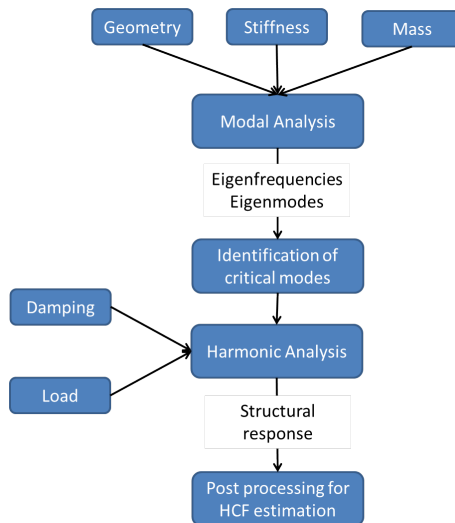


Figure 2: *Process map for an HCF estimation.*

1.4 Limitations

Several limitations and simplifications had to be made during all stages of the thesis and are covered continuously in the report. More general limitations are:

- Only a sandwich design with the specific CFRE/foam material system used in GKN's current OGV concept is analysed.
- Only the material damping of the structure is investigated, i.e., external damping originating from e.g., the interface to the FHF and AFC for the real OGV is not covered.
- Experimental testing is done in-house at GKN which means that the performed tests are limited to the available resources.
- The sandwich test pieces are manufactured by Applied Composites AB (ACAB), which is a subsidiary of GAES. Limitations in tooling and cost set boundaries on the design, size and number of test pieces.
- All Finite Element Analysis (FEA) is made using ANSYS[®] 14.0 and are therefore limited to the capability of that specific software and version.

1.5 Scope of work

Initial work in the thesis covered the design of the test set-up and the CFRE/foam sandwich specimen geometry used for experimental testing. The work continued with a theoretical study of micromechanics and viscoelasticity and their implementations for orthotropic composite materials. The knowledge gained from the theory was applied on the determination of the damping properties of the constituent materials in the sandwich composite. The continued work was then focused on the homogenisation of the constituent damping using micromechanics. As a final step in developing the method, the implementation of the orthotropic damping of the composite in ANSYS[®] was covered. The prediction of the composite damping using the developed method was finally validated against results from both literature and experimental testing.

CAD geometry and drawings were made using CATIA[®] V5R19 due to earlier experience in that specific software and the available student license at Chalmers.

FE pre-processing was done using HyperMesh[®] 11.0 while the numerical calculations were performed using ANSYS[®] 14.0 and the results were post-processed using HyperView[®] 11.0 and MATLAB[®] R2011a. These softwares were chosen since they are tools commonly used at GAES which means that the developed method can be easily implemented.

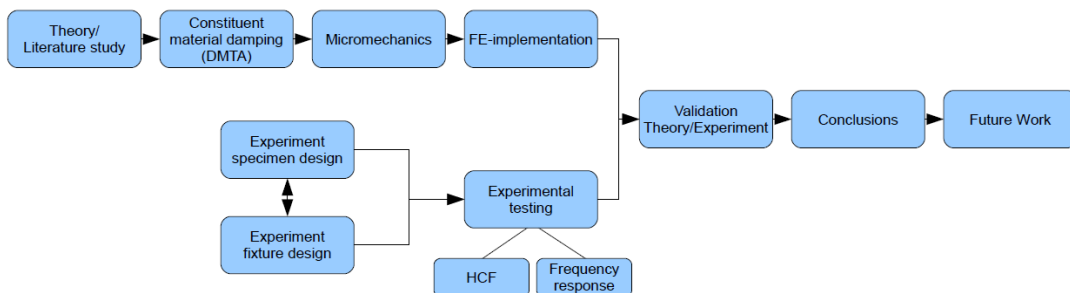


Figure 3: *Process map for the thesis.*

2 Damping - prediction & implementation

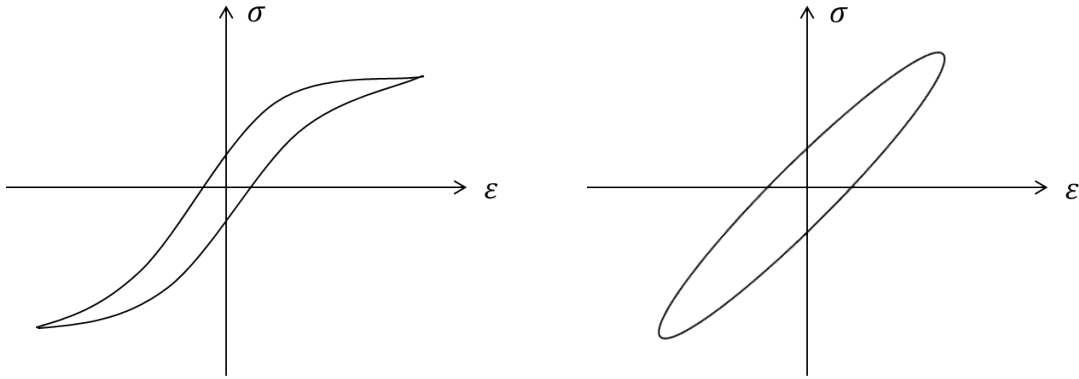
Damping is a measure of the amount of dissipated energy in a vibrating structure. There are different types of external damping mechanisms in a structure, e.g., acoustic radiation damping or Coulomb friction etc. The focus in this thesis however is on internal material damping.

2.1 Basic concepts in damping

The internal damping behaviour of a material can be observed by examining the stress versus strain curve during harmonic excitation, the so-called hysteresis curve. A general hysteresis curve for a nonlinear material can be seen in Figure 4a. The area inside this loop is equivalent to the energy dissipated per load cycle

$$\Delta U = \oint \sigma d\epsilon \quad (1)$$

For a general nonlinear material the shape of the hysteresis loop is a nonlinear function of temperature, frequency and stress amplitude. As a simplification of the general nonlinear behaviour linear viscoelasticity is often assumed. Elastic materials respond instantaneously to an applied stress. Viscoelastic materials also exhibit this behaviour but in addition they also have a delayed response. For a viscoelastic material, a harmonically varying stress causes a harmonic strain response but with a phase lag, δ . For linear viscoelastic materials there is a linear relation between stress and strain and because of the phase lag the hysteresis loop take an elliptical shape seen in Figure 4b. The energy lost in each loading cycle corresponds to the area in the ellipse which for a given applied



(a) *Hysteresis loop for general nonlinear material.*

(b) *Hysteresis loop for linear viscoelastic material.*

Figure 4: *Hysteresis loops for different materials during harmonic excitation.*

stress $\sigma(t) = \sigma_0 \sin(\omega t)$ and corresponding structural strain response $\epsilon(t) = \epsilon_0 \sin(\omega t + \delta)$ is given by

$$\Delta U = \int_0^T \sigma(t) \frac{d\epsilon(t)}{dt} dt = \int_0^T (\sigma_0 \sin(\omega t)) (\omega \epsilon_0 \cos(\omega t + \delta)) dt = \pi \sigma_0 \epsilon_0 \sin(\delta) \quad (2)$$

With the strain energy in the structure defined as the energy stored from zero force and displacement to the point of maximum displacement

$$U = \frac{1}{2} \left(\epsilon_0 \sin \left(\frac{\pi}{2} \right) \right) \left(\sigma_0 \sin \left(\frac{\pi}{2} - \delta \right) \right) = \frac{1}{2} \sigma_0 \epsilon_0 \cos(\delta) \quad (3)$$

Then the following relation is true

$$\tan(\delta) = \frac{\Delta U}{2\pi U} \quad (4)$$

which means that the so called loss tangent, $\tan(\delta)$, of a linear viscoelastic material can be used as a measure of its damping.

The general time-dependent stress-strain relation for a viscoelastic material is given by the Boltzmann superposition principle on integral form [6]

$$\sigma_{ij}(t) = \int_{-\infty}^t C_{ijkl}(t-\tau) \frac{d\epsilon_{kl}(\tau)}{d\tau} d\tau \quad (5)$$

where $C_{ijkl}(t)$ is the relaxation stiffness matrix. In the special case of steady state harmonic oscillations, Eq. (5) can with the use of the Fourier transform and Voigt notation be written as

$$\sigma_i(t) = C_{ij}^*(\omega) \epsilon_j(t) \quad (6)$$

where C_{ij}^* is the complex dynamic stiffness

$$C_{ij}^* = C'_{ij}(\omega) + iC''_{ij}(\omega) = C'_{ij}(\omega)(1 + i\eta_{ij}) \quad (7)$$

and

$$\eta_{ij} = \tan(\delta_{ij}) = \frac{C''_{ij}}{C'_{ij}} \quad (8)$$

The real part of the complex modulus, C'_{ij} , is called the storage modulus and is associated with the elastic energy storage in the material. The imaginary part, C''_{ij} , on the other hand is called the loss modulus and is associated with the energy dissipation, i.e., damping, in the material. The relation between the two moduli and the material damping is given by Eq. (8). The term loss tangent, $\tan(\delta)$, only has a physical meaning for linear viscoelastic materials and the more general term loss factor, η , is often used instead. When comparing the static constitutive relation, $\sigma_i = C_{ij} \epsilon_j$, with the dynamic counterpart in Eq. (6) the similarities are clear. By simply replacing the static modulus, C_{ij} , with the complex dynamic modulus, C_{ij}^* , it is possible to convert an elastic equation to a steady state harmonic viscoelastic equation. This principle is called the elastic-viscoelastic correspondence principle. The application of the correspondence principle on composite materials was developed in the 1950s and the most important implication is that analytical models for prediction of elastic material properties can be used to find the corresponding viscoelastic material properties[11].

2.1.1 Experimental damping characterisation

When experimentally characterising the damping of a structure it is not customary to use hysteresis curves as the ones seen in Figure 4. Instead the damping is often determined using one of the two methods described below.

Logarithmic decrement method

This method uses the free vibration decay curve of a structure, obtained after the removal of the excitation source. An example of such a decay curve can be seen in Figure 5. The logarithmic decrement can be calculated from the decay curve as

$$\Delta = \frac{1}{n} \ln \left(\frac{x(t)}{x(t+nT)} \right) \quad (9)$$

where $x(t)$ is the peak amplitude at time t and $x(t+nT)$ is the peak after an additional n periods. The relation between the logarithmic decrement and other common damping measures can be found in Section 2.1.2.

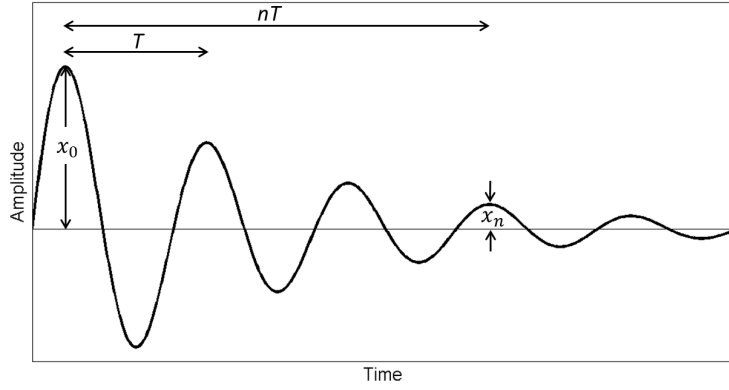


Figure 5: *Free vibration decay curve*

Half-power bandwidth method

This method uses the frequency response spectrum obtained from a forced vibration test, as the one from a Single-Degree-Of-Freedom (SDOF) system seen in Figure 6. The damping for eigenmode i can be calculated from this spectrum as

$$\eta_i = \frac{\Delta\omega_i}{\omega_i} = \frac{\omega_2 - \omega_1}{\omega_i} \quad (10)$$

where $\Delta\omega_i$ is the half-power bandwidth and ω_i is the eigenfrequency of mode i . The linear spectrum is shown in figure 6 and not the power spectrum which means that the half-power points are found at $x_{max}/\sqrt{2}$.

A benefit with the half-power bandwidth method is that the damping for several eigenmodes can be calculated from a single frequency response spectrum whereas the logarithmic decrement method requires separate decay curves for each mode.

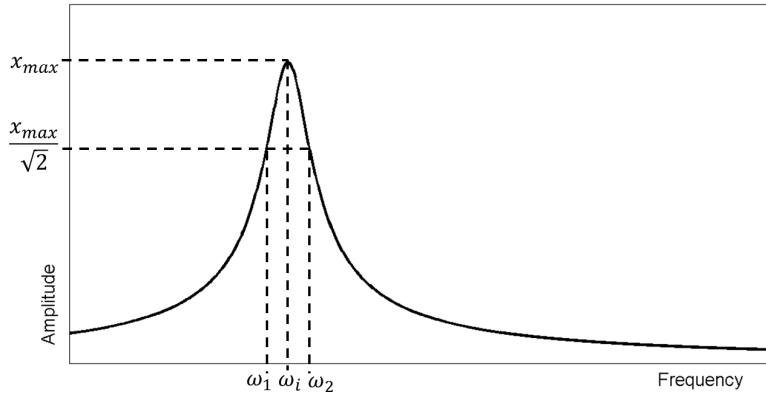


Figure 6: *Frequency response spectrum*

2.1.2 Measures of damping

There exist different measures to quantify damping, some of which has already been introduced in the sections above. The loss factor quantity, η , is a commonly used measure and will be used consistently throughout the report. The loss factor is related to other common damping measures as

$$\eta = \tan(\delta) = 2\zeta = \frac{\Psi}{2\pi} = \frac{\Delta}{\pi} \quad (11)$$

where

η = loss factor

$\tan(\delta) = \frac{E''}{E'}$ = loss tangent

ζ = damping ratio

$\Psi = \frac{\Delta U}{U}$ = Specific Damping Capacity (SDC)

Δ = logarithmic decrement

2.2 Composite damping

The internal material damping in conventional metallic materials is very low which means that they dissipate energy mainly through external damping mechanisms. Composite materials on the other hand have high inherent damping on a macroscopic scale and have other damping mechanisms than metallic materials.

2.2.1 Damping mechanisms in composites

The primary source of internal material damping in a composite lamina is the viscoelastic behaviour of the matrix and fibre. In [1] it was shown that carbon fibre filaments have very low damping and therefore can be assumed to be purely elastic. This means that the majority of the damping for a CFRE composite is originating from the matrix material. As for the elastic properties of the composite, the damping is orthotropic and is influenced by the relative proportions of matrix and fibre and the orientation of the fibres relative to the applied loading. External factors such as frequency, temperature and vibrational amplitude can also have an effect on the damping. In [23] however, it was concluded that CFRE have damping properties that are independent of vibration amplitude at lower levels, and have a frequency dependence which is minor when well below the glass transition temperature of the matrix. Nonlinear damping is only experienced in damaged composites or at large stress amplitudes.

The matrix material immediately surrounding the fibre can have properties that are significantly different from those of the bulk matrix. This so called interphase can be either weaker or stronger than the bulk matrix and is believed to be caused by the interaction between the matrix hardener and the fibre surface treatment. In [13] the effect of a fibre-matrix interphase on the damping of composites was investigated using a micromechanical Finite Element (FE) approach on a Representative Volume Element (RVE). There it was assumed that the interphase is isotropic and has properties that can be estimated as an average of fibre and matrix properties. By changing the volume fraction of the interphase, its effects on composite damping could be studied. The analysis showed that the contribution from the interphase to the total damping when the load is applied in fibre direction is negligible and the fibre damping is the most significant. The same was shown for the transverse damping where the interphase has negligible effect and the matrix damping is most significant instead. However, the opposite was found for the in-plane shear damping where the interphase had a major contribution while the shear modulus was kept unaffected. This shows that the properties of the interphase can have a large effect on the damping of the composite. One major problem with implementing the interphase as a third phase in a micromechanical model is the experimental determination of its properties.

Although the carbon fibre has negligible damping by itself it may have significant effect on the damping due to its interface to the matrix. Microscopical damages at the interface can cause slip between matrix and fibre and an increase in damping while the stiffness is unaffected [26].

When looking at the composite damping on a laminate level additional damping mechanisms can arise, like interlaminar stresses. The conventional Classical Laminate Theory (CLT) used for homogenisation of laminates is based on the assumption of plane stress which means that it neglects the interlaminar stresses and will give more or less inaccurate prediction of the damping. The interlaminar stresses for thin laminates are minor and First-order Shear Deformation Theory (FSDT) is sufficient to get accurate results for both damping and stiffness[24],[14]. For thick laminates

however, the interlaminar stresses are more pronounced and have a great influence on damping. In the same way that FSDT overestimates the stiffness of thick laminates it gives a too low value of the damping since it underestimates the transverse shear. In [18] it is stated that the transverse effect become dominant at a length-to-thickness ratio of ~ 20 for a simply supported $[0/90]_s$ laminate. It is also stated that the effect of fibre orientation and lay-up on damping diminishes for thick laminates since the shear deformation is the main source of damping for all fibre orientations. The actual shear deformation may be small but the contribution to damping can be significant due to a high interlaminar loss factor. To accurately model the interlaminar effect using FEA one would need to explicitly model each discrete lamina and interlaminar region of the laminate. In [24] a 13 Degree Of Freedom (DOF) per node element was introduced, based on Higher-order Shear Deformation Theory (HSDT) that accounts for the discontinuity at the lamina interfaces. This approach is more efficient than explicit modelling of each interface since the DOFs do not increase with an increase in number of lamina. However, this type of HSDT element is not available in any commercial FE-software. In [24] it is also stated that HSDT is needed for even moderately thin sandwich laminates for accurate prediction of stiffness and damping, which is in agreement with the findings in [22]. In [14] it is stated that the effect of interlaminar damping due to the free-edge-effect is proportional to the size of the boundary layer in relation to the total size of the laminate. The size of the boundary layer is usually said to be of the same order as the laminate thickness. No micromechanical theory for the prediction of the interlaminar damping has been found but since the matrix is the bonding material between the different laminae it can be assumed that the interlaminar loss factor is similar to that of the matrix [31].

2.2.2 Dynamic Mechanical Thermal Analysis of neat resin

In 2008 the company Swerea SICOMP performed so called Dynamic Mechanical Thermal Analysis (DMTA) on the neat epoxy resin used in the GKN material system to determine its viscoelastic properties. The test was done in a three point bending set-up where the specimen was excited at six frequencies $\log_{10}(f) = [-\frac{1}{3}, 0, \frac{1}{3}, \frac{2}{3}, 1, \frac{4}{3}]$ for every 10°C in a temperature sweep from -50°C to 250°C . The raw data recorded during the DMTA were processed in a supplied Excel[®]-sheet from Swerea SICOMP which returns the storage modulus and loss factor for each specific temperature and frequency. The raw data of the storage modulus for one of the resin test pieces can be seen in Figure 7.

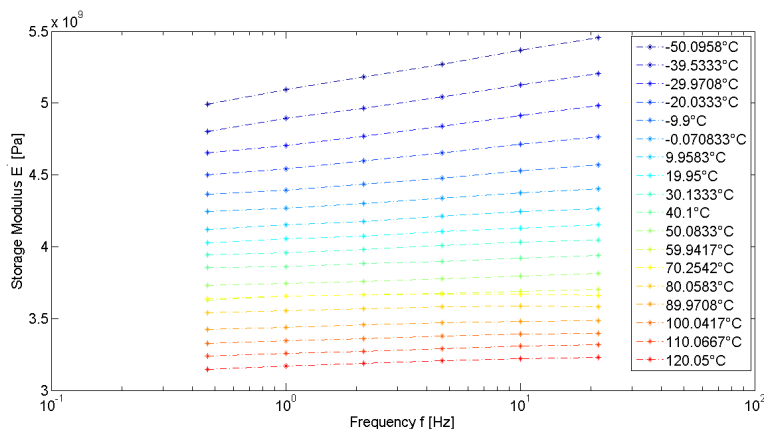


Figure 7: Raw data of storage modulus, E' .

Testing an even broader range of temperatures and frequencies than the ones stated above would increase the testing time considerably and put higher demands on the testing equipment. Fortunately so called master curves can be derived for linear viscoelastic materials using the time-temperature superposition principle. The principle is based on the assumption that a modulus at one specific frequency and temperature is identical to the modulus at another specific frequency-temperature combination [15]

$$E(f_1, T_1) = E(\alpha(T_2)f_1, T_2) \quad (12)$$

where $\alpha(T)$ is the so called shift factor. The shift factor as a function of temperature is for known material constants given by analytical expressions like the WLF or Arrhenius equations [15]. In this case however when only experimental data is available, the easiest way to determine the shift factor is by manually shifting the data relative to a chosen reference to create a continuous master curve. This means that the raw data from the test, available at only a limited range of temperatures and frequencies, can be shifted to cover a broader spectrum. The resulting master curve after performing such a shift for the storage modulus at 20°C can be seen in Figure 8. The viscoelastic behaviour is clear already at this low temperature far from the glass transition temperature at 183°C. Some difference in stiffness between the four test pieces tested is evident, but the individual master curves are stable which supports that the experimental results can be trusted. The values correspond well with the values from the manufacturer and another independent static test [25],[7]. The difference in modulus between the test pieces could be due to actual difference in properties between the samples. However, the test set-up used is sensitive to the clamping of the specimen as well as the force and amplitude used to drive the motion and makes for a more likely reason of the scatter in data. The 1Hz – 1kHz region is the interesting region in the current work. Although the modulus is clearly not constant in this region only a $\sim 5\%$ increase compared to the static value in [7] can be observed.

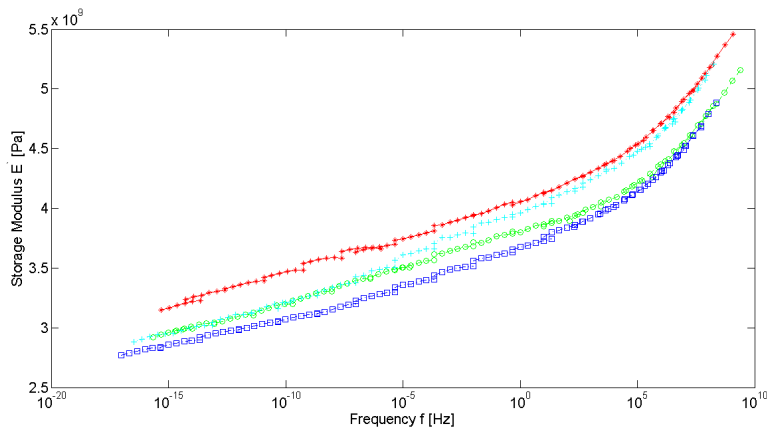


Figure 8: *Master curve of storage modulus, E' , at 20°C for the four test pieces.*

The shift factor, α , for all four test pieces as a function of the relative temperature to the 20°C reference temperature can be seen in Figure 9. Ideally, the shift factors for the different test pieces should be identical. This is clearly not the case but for the frequency region of interest, which corresponds to a relative temperature of -20°C in the figure, the difference is deemed acceptable. Some part of the difference is caused by the shift factor being determined manually for each test specimen to create a continuous master curve which is done in a subjective way.

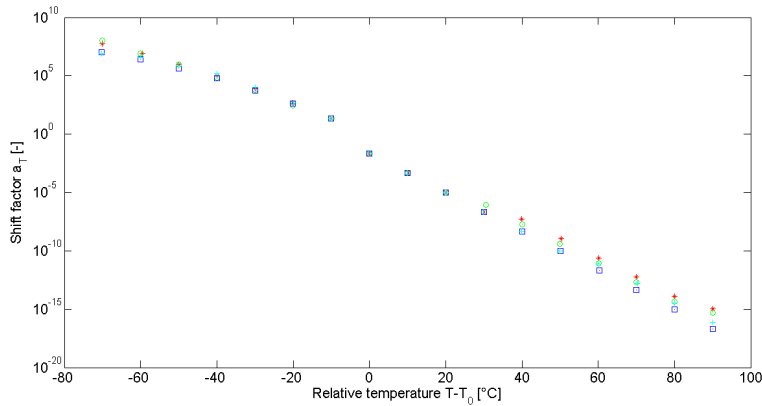


Figure 9: *Shift factor, α , as function of relative temperature to the reference for the four test pieces.*

Applying the shift factors in Figure 9 on the loss factor data gives the master curves seen in Figure 10. The data on the loss factor is clearly not as stable as those on the storage modulus and the difference between the individual test pieces is also larger. This is an indication that the damping measurement is sensitive to the clamping of the test specimen since it can introduce extraneous damping. The frequency dependence in the 1Hz – 1kHz region is clearly minor and can be approximated by the constant value $\eta \approx 0.04$. Rate-independent linear damping can be observed in polymers over a limited temperature and frequency range remote from those at the transition region according to [20] which is the case here. The data supplied by the resin manufacturer also suggest an almost rate-independent damping for temperatures below the transition temperature but at a much higher level $\tan(\delta) \approx 0.1$ [25].

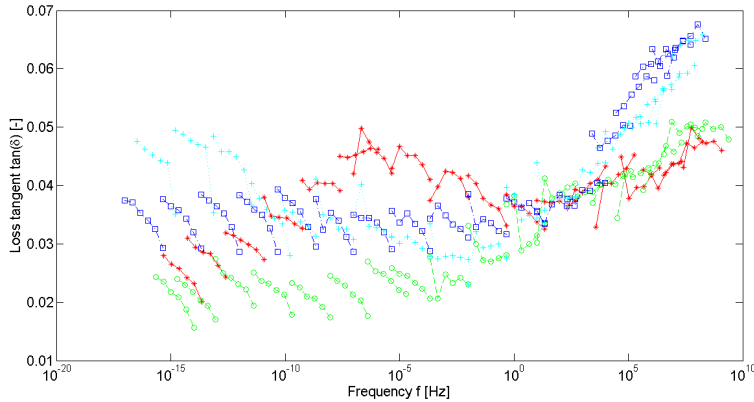


Figure 10: *Loss tangent, $\tan(\delta)$, for the four test pieces.*

The DMTA was performed in flexure and gave the dynamic tensile modulus, E^* . To fully describe an isotropic material two material properties are needed, which means that another dynamic modulus of the resin has to be determined. The difference in loss factor between extension and shear however, is in most cases unmeasurable and $\eta_E \approx \eta_G$ is assumed [11],[5]. This means that $\eta_\nu = 0$ and there is no phase lag between an applied strain and the strain caused by the Poisson effect, which is reasonable for at least moderate frequencies. Damping in polymers is usually assumed to result from only shear deformation and no damping occur in bulk deformation. This gives the relation between the two loss factors as [21]

$$\eta_E = \frac{2\eta_G K}{G(1 + \eta_G^2) + K} \approx 0.037 \quad (13)$$

where K is the bulk modulus. Given the small difference in loss factor, the assumption of $\eta_E \approx \eta_G$ is therefore reasonable.

2.2.3 Prediction of composite damping

The unique properties of a composite material are caused by the complex interaction between its constituent materials. The principal of micromechanics is that the properties of the constituents in a heterogeneous material can be related to an equivalent homogeneous material. The general formula for the homogenisation of the stiffness of a two-phase composite is given by

$$\mathbf{C}_c = \mathbf{C}_m(\mathbf{I} - \phi\mathbf{A}) + \phi\mathbf{C}_f\mathbf{A} \quad (14)$$

where ϕ is the fibre volume fraction and \mathbf{A} is the Eshelby's tensor. The Eshelby's tensor relates the average strain in the inclusion, in this case the fibre, to the average strain in the homogeneous composite material as

$$\epsilon_f = \mathbf{A}\epsilon_c \quad (15)$$

Analytical expressions for the Eshelby's tensor is only available for simplified geometries which means that Eq. (14) in general cannot be solved. Instead more or less detailed micromechanical models have been developed to approximate the properties of the homogenised material. Most models are based on either a rather simple mechanics of materials approach, a more complex elasticity theory or empirical solutions made to fit experimental data [27].

The Halpin-Tsai equations is a well-known and widely used semi-empirical micromechanical model and is given by

$$\frac{p_c}{p_m} = \frac{1 + \zeta\eta v_f}{1 - \eta v_f} \quad (16)$$

$$\eta = \frac{\frac{p_f}{p_m} - 1}{\frac{p_f}{p_m} + \zeta} \quad (17)$$

where p_c is a composite modulus, p_f is a fibre modulus, p_m is a matrix modulus and v_f is the fibre volume fraction. ζ is an empirically determined parameter dependent on loading condition as well as fibre geometry and packing. The equations form an interpolation that approximate more complicated micromechanical models. It can be shown that when $\zeta = 0$ and $\zeta = \infty$, the Halpin-Tsai equations reduce to the Inverse Rule Of Mixtures (IROM) and the Rule Of Mixtures (ROM) respectively which are the lower and upper bound on the composite modulus [11]. When extending the micromechanical approach to also include damping, one can simply make use of the correspondence principle described in Section 2.1.

The carbon fibre filament is assumed to be transversely isotropic with the axis of symmetry along the fibre direction while the matrix is assumed to be isotropic. This means that the composite lamina will be transversely isotropic. The strain-stress relation for this type of material is given by

$$\begin{bmatrix} \epsilon_1 \\ \epsilon_2 \\ \epsilon_3 \\ \gamma_{23} \\ \gamma_{13} \\ \gamma_{12} \end{bmatrix} = \begin{bmatrix} \frac{1}{E_1} & -\frac{\nu_{12}}{E_1} & -\frac{\nu_{12}}{E_1} & 0 & 0 & 0 \\ -\frac{\nu_{12}}{E_1} & \frac{1}{E_2} & -\frac{\nu_{23}}{E_2} & 0 & 0 & 0 \\ -\frac{\nu_{12}}{E_1} & -\frac{\nu_{23}}{E_2} & \frac{1}{E_2} & 0 & 0 & 0 \\ 0 & 0 & 0 & \frac{2(1+\nu_{23})}{E_2} & 0 & 0 \\ 0 & 0 & 0 & 0 & \frac{1}{G_{12}} & 0 \\ 0 & 0 & 0 & 0 & 0 & \frac{1}{G_{12}} \end{bmatrix} \begin{bmatrix} \sigma_1 \\ \sigma_2 \\ \sigma_3 \\ \sigma_{23} \\ \sigma_{13} \\ \sigma_{12} \end{bmatrix}, \epsilon = \mathbf{S}\sigma \quad (18)$$

With the inverse relation

$$\sigma = \mathbf{S}^{-1}\epsilon = \mathbf{C}\epsilon \quad (19)$$

This means that five independent engineering constants, $E_1, E_2, G_{12}, \nu_{12}$ and ν_{23} , is needed to describe the material. These engineering constants has earlier been determined through experimental testing for the GKN material system and can be found in [28]. For the isotropic resin, the two engineering constants E and ν has also been determined through experimental testing and can be found in [7].

For the carbon fibre filament only the longitudinal stiffness, E_1 , is known from the manufacturer [9] because of the difficulty to determine the other properties of a single fibre filament. Therefore, the remaining four engineering constants needed to fully describe the fibre material has to be deduced from the known composite and matrix properties using e.g., the Halpin-Tsai equations. The limited

data available for the composite at only one given fibre volume fraction makes it impossible and also unnecessary to use a more complicated micromechanical model than the Halpin-Tsai equations.

The Halpin-Tsai equations, and other micromechanical models, are normally used to calculate unknown composite properties from known fibre and matrix data. By rewriting Eq. (16) and (17) to the form in Eq. (20) and (21) the micromechanical model can instead be used to calculate the unknown fibre properties from the already known composite and matrix properties.

$$\eta = \frac{\frac{p_c}{p_m} - 1}{v_f \left(\frac{p_c}{p_m} \right)} \quad (20)$$

$$p_f = \frac{p_m (1 + \zeta \eta)}{1 - \eta} \quad (21)$$

For a composite with oriented continuous circular fibres Halpin suggests the assumption of equal strain condition in fibre and matrix, i.e., Voigt-assumption, when calculating ν_{12} and E_{11} . This gives the simple ROM formulas [12]

$$E_{f_1} \cong \frac{E_{11} - E_m(1 - v_f)}{v_f} \quad (22)$$

$$\nu_{f_{12}} \cong \frac{\nu_{12} - \nu_m(1 - v_f)}{v_f} \quad (23)$$

The longitudinal fibre modulus, E_{f_1} , derived in this way from composite and matrix data gives a modulus that is 90% of the stiffness stated by the manufacturer. The lower stiffness in the composite is most likely caused by e.g., micro scale defects and fibre misalignment. The lower stiffness is assumed to describe the material more accurately than the more ideal single fibre filament stiffness.

When calculating longitudinal shear stiffness, G_{12} , and the transversal stiffness, E_{22} , Halpin states that Eq. (16) and (17) should be used with $\zeta = 1$ and $\zeta = 2$ respectively. However, when calculating the out of plane shear stiffness, $G_{f_{23}}$, he suggests that

$$\zeta \cong \frac{1}{4 - 3\nu_m} \quad (24)$$

should be used. However, when inserted in Eq. (21) together with the available material data there is no solution. If instead the same value as for E_{22} , $\zeta = 2$, is used a solution can be found. This is a reasonable assumption given that the material is transversely isotropic and the deformation in both cases is mostly matrix dependent. In our case the explicit calculation of $G_{f_{23}}$ is actually unnecessary since transverse isotropy has been assumed which allows $G_{f_{23}}$ to be calculated as

$$G_{f_{23}} = \frac{E_{f_2}}{2(1 + \nu_{f_{23}})} \quad (25)$$

With the elastic properties of both matrix and fibre fully defined it is now possible to introduce the damping in the matrix found in Section 2.2.2. Replacing the static matrix modulus in Eq. (16) and (17) with the dynamic counterpart, in accordance with the correspondence principle, it is possible to calculate the dynamic moduli of the composite. The transversely isotropic loss factors found for the composite using this procedure are summarised in Table 1. The damping in the fibre direction, η_{E_1} , is close to zero. This is not surprising given that the stiffness and deformation in this direction is mostly fibre dependent, which from the beginning was assumed to have zero damping. Loading in transverse direction and in shear on the other hand is mostly matrix dependent and gives damping values for the composite which are closer to that of the matrix at 4%.

Table 1: Damping properties of composite

η_{E_1}	η_{E_2}	$\eta_{G_{12}}$	$\eta_{\nu_{12}}$	$\eta_{\nu_{23}}$
0.04%	2.41%	3.73%	0%	0%

The loss factors in Table 1 are the values for a given 1D stress state. For the more general 3D stress state the constitutive relation is given by Eq. (6) and the loss factor matrix is

$$\eta_{ij} = \begin{bmatrix} 0.10 & 2.47 & 2.47 & 0 & 0 & 0 \\ 2.47 & 2.45 & 2.51 & 0 & 0 & 0 \\ 2.47 & 2.51 & 2.45 & 0 & 0 & 0 \\ 0 & 0 & 0 & 2.41 & 0 & 0 \\ 0 & 0 & 0 & 0 & 3.73 & 0 \\ 0 & 0 & 0 & 0 & 0 & 3.73 \end{bmatrix}$$

Given the orthotropic behaviour of the CFRE it is possible to design a structure for maximum damping. However, the damping is nearly inversely proportional to the stiffness, as seen in Figure 11, which means that there is a trade-off between stiffness and damping.

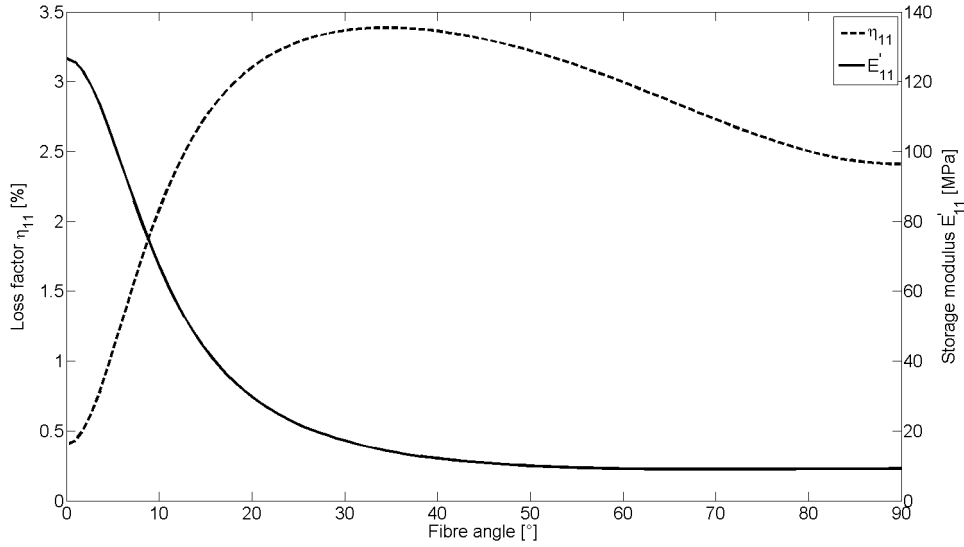


Figure 11: Loss factor, η_{11} , and storage modulus, E'_{11} , as function of fibre orientation.

2.2.4 FE implementation

To be able to use the predicted damping properties of the CFRE in an HCF estimation, it must be able to be implemented in an FE environment. When performing a harmonic analysis in ANSYS® the damping matrix is constructed as the sum of the following components [3]

$$[C] = \alpha[M] + \left(\beta + \frac{2}{\Omega}g\right)[K] + \sum_{i=1}^{N_{ma}} \alpha_i^m [M_i] + \sum_{j=1}^{N_m} \left[\left(\beta_j^m + \frac{2}{\Omega}g_j + \frac{1}{\Omega}g_j^E \right) [K_j] \right] \quad (26)$$

where

- $[C]$ = structure damping matrix
- α = mass matrix multiplier
- $[M]$ = structure mass matrix
- β = stiffness matrix multiplier
- g = constant structural damping ratio
- Ω = excitation circular frequency
- $[K]$ = structure stiffness matrix
- N_{ma} = number of materials with α_i^m input
- α_i^m = stiffness matrix multiplier for material i

- $[M_i]$ = portion of structure mass matrix based on material i
- N_m = number of materials with β_j^m , g_j or g_j^E input
- β_j^m = stiffness matrix multiplier for material j
- g_j = constant structural damping ratio for material j
- g_j^E = material damping coefficient

As seen in Eq. (26) the damping can only be constructed as a factor multiplied to either the global stiffness or mass matrix, $[K]$ and $[M]$, or on a material basis, $[K_j]$ and $[M_i]$. There is a possibility to define complex material data in ANSYS[®] 14.0 but that functionality is limited to isotropic materials [2]. For the foam damping this is not an issue since the material is isotropic and the loss modulus is simply a factor of the storage modulus, i.e., the loss factor. For the CFRE this is problem however, since it has orthotropic damping and different loss factors in the different directions of the material. Simply defining its damping as a factor of its stiffness would only give the right damping in one direction and give either an under- or overestimation in the other directions. A way to circumvent this limitation in damping matrix formulation is by using two separate elements for the stiffness and damping, i.e., storage moduli and loss moduli, but making them coincident and sharing the same nodes. This will make it possible to create the correct damping matrix by only adding the contribution from the loss moduli element. However, when assembling the global stiffness matrix it will now consist of the contribution from both elements. Scaling down the loss moduli and instead compensating with a large damping factor when constructing the damping matrix in Eq. (26) the contribution from the second element to the overall stiffness can be made negligible.

The functionality of this method was proven by performing a substructure analysis in ANSYS[®], comparing the stiffness and damping matrices created when using two coincident elements instead of a single element. The resulting matrices for different values of the scaling of the second elements stiffness can be seen in Figure 12. The correct damping matrix is always created but the error in the stiffness matrix is dependent on the scaling factor used. From the figure it is clear that the global stiffness matrix consist of the combined stiffness from the two elements $[K] = [K_1] + [K_2]$. For example when a scaling factor of 0.5 is used, the global stiffness is $[K] = [K_1] + 0.5[K_1] = 1.5[K_1]$ which normalised gives the value 1.5. The error in the stiffness matrix is therefore simply proportional to the scaling of the second elements stiffness, i.e., scaling with a factor of 10^{-3} will give an error of only 0.1% in the stiffness matrix. The same reasoning is valid regarding the mass matrix, $[M] = [M_1] + [M_2]$. A density should be specified for all elements during a dynamic analysis but by simply setting a low enough density for the loss moduli element the error in the mass matrix can be made negligible.

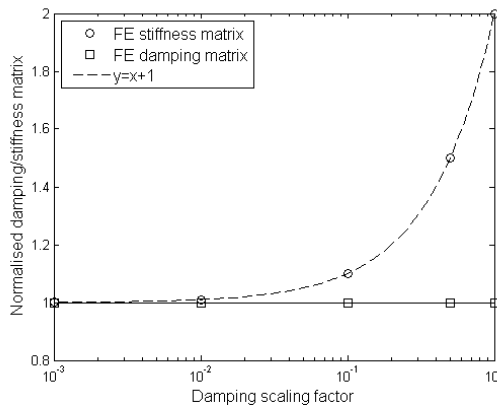


Figure 12: Magnitude of global stiffness and damping matrices as function of the scaling of the loss moduli element.

When separating the complex stiffness C^* of the material into two separate materials it has to be remembered that

$$C^*(E^*) \neq C'(E') + iC''(E'') \quad (27)$$

This means that the orthotropic loss moduli data for the loss moduli element cannot simply be taken as the individual modulus in each direction but has to be back-calculated from the imaginary part of the true loss stiffness matrix $C^*(E^*)$.

As for an isotropic material there are thermodynamic constraints on the engineering constants for an orthotropic material. These constraints translate to that the stiffness and compliance matrices has to be positive-definite which ensures that the strain energy is positive, i.e., energy is consumed during deformation [16]. This always has to be tested when using experimental material data to make sure that they are physically possible. This test is also important in this case since the composite loss moduli have been transformed into a separate elastic moduli which cannot be guaranteed to comply with these rules. In ANSYS® this is tested by assuring that the determinant of the matrix is positive [3]

$$1 - (\nu_{xy})^2 \frac{E_y}{E_x} - (\nu_{yz})^2 \frac{E_z}{E_y} - (\nu_{xz})^2 \frac{E_z}{E_x} - 2\nu_{xy}\nu_{yz}\nu_{xz} \frac{E_z}{E_x} > 0 \quad (28)$$

Only one damping factor can be assigned per element in ANSYS® and is decided by the material type assigned to the element as a whole. This will cause problem when using multiple-material elements, e.g., SOLSH190 or SOLID185, and trying to model multiple materials with different damping in a single element. The reason for this is that the element damping matrix is calculated as a factor of the element stiffness matrix and not of its constituents. This is not a problem when modelling composite layers of different orientations since the element still only consist of one type of material. However, this makes it impossible to model the damping of a complete sandwich structure using only one element through the thickness.

The equation of motion for an undamped discrete system is given by

$$\mathbf{M}\ddot{\mathbf{x}} + \mathbf{K}\mathbf{x} = \mathbf{F} \quad (29)$$

which for a harmonic excitations $\mathbf{F} = \mathbf{F}_0 e^{i\omega t}$ and harmonic response $\mathbf{x} = \mathbf{x}_0 e^{i\omega t}$ can be rewritten as

$$-\omega^2 \mathbf{M}\mathbf{x}_0 + \mathbf{K}\mathbf{x}_0 = \mathbf{F}_0 \quad (30)$$

Using the correspondence principle and replacing the elastic stiffness with the viscoelastic stiffness the equation can be written as

$$-\omega^2 \mathbf{M}\mathbf{x}_0 + \mathbf{iK}''\mathbf{x}_0 + \mathbf{K}'\mathbf{x}_0 = \mathbf{F}_0 \quad (31)$$

Comparing Eq. (31) to the regular equation for a damped system

$$-\omega^2 \mathbf{M}\mathbf{x}_0 + \mathbf{i}\omega \mathbf{C}\mathbf{x}_0 + \mathbf{K}\mathbf{x}_0 = \mathbf{F}_0 \quad (32)$$

it is clear that the following relation must be true

$$\mathbf{C} = \frac{\mathbf{K}''}{\omega} \quad (33)$$

Looking at the expression for the damping matrix in Eq. (26) the most suitable choice of damping factor when constructing the damping matrix is to use the so called constant damping ratio $[C] = \frac{\eta}{\omega} [K]$.

2.2.5 Method summary

The following section serve as a summary of the necessary steps in the prediction and implementation of the composite damping covered in Sections 2.2.2-2.2.4. The complete process map can be seen in Figure 13.

As a prerequisite, the developed method requires completely defined elastic properties for a composite ply. In the current case transverse isotropy was assumed which means that five independent engineering constants have to be determined experimentally. In addition to composite data, the method also requires known elastic and dynamic properties of the resin material. The resin is isotropic which means that two independent engineering constant has to be determined

through e.g., DMTA. Single fibre filament data is rarely available and is therefore determined from the known composite and resin properties through a micromechanical model, in this case the Halpin-Tsai model. The newly determined fibre properties can now, thanks to the correspondence principle, be used together with the known resin properties in the Halpin-Tsai micromechanical model to determine the dynamic properties of the composite ply. Since the complex orthotropic dynamic properties of the composite cannot be input in ANSYS® directly it is separated into its real and imaginary components which are then input to their individual element.

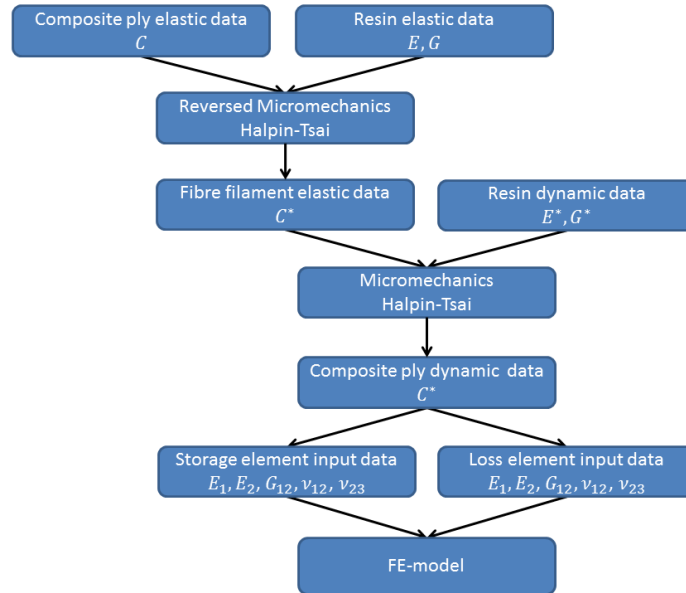


Figure 13: Process map describing the different steps in the prediction and FE-implementation of the composite damping.

2.2.6 Validation of method against literature results

To validate the capability of the developed method a validation against the experimental results in Reference [5] was made. The paper covers the experimental testing of the damping of off-axis glass and Kevlar cantilever beams in their first flexural mode of vibration for fibre orientations of 0° , 15° , 30° , 45° , 60° , 75° and 90° . The beams were made in size of $180 \times 20 \times 2.5$ mm and made using SR1500 epoxy resin with SD2505 hardener together with E-glass and Kevlar fibre respectively. The engineering constants, E_1 , E_2 , G_{12} , ν_{12} for both composites are stated in the paper. The missing poisson ratio, ν_{23} , is assumed to be the same as for the GKN material system in [28]. There is a lack of DMTA data for The SR1500/SD2505 epoxy system, but since its density and elastic properties are in good agreement with those of the resin described in Section 2.2.2 it is a reasonable initial assumption that their damping are the same. Prediction of the composite complex moduli can now be made following the procedure covered in Section 2.2.3.

The beam is modelled in ANSYS® using $36 \times 4 \times 4$ (LxWxH) SOLSH190 elements and can be seen in Figure 14. The different laminae orientations tested in the paper is modelled by changing the element coordinate systems in step of 15° . The impact test used in the paper is simulated in

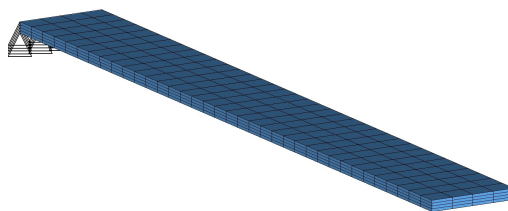


Figure 14: Cantilever FE-model

ANSYS[®] using a harmonic analysis with a forced harmonic excitation of the clamped end. The damping of the beam is determined using the half power bandwidth from the frequency response of the first flexural mode, which is the same method used on the experimental results in the paper. The experimental results from the paper together with the numerical results can be seen in Figure 15a. It is clear that the assumed matrix damping overpredicts the total structural damping for all orientations except for the fibre dominated 0° orientation. Rerunning the analysis with a matrix damping of 1.75% which is closer to the experimental values, one gets the results seen in Figure 15b. The magnitude of the damping is now closer to the experimental values but the damping is underestimated for both 0° and 90° orientations. This is an indication that the assumption of zero damping in the fibre might be incorrect. Figure 15c shows the results from a third analysis where the damping parameters have been adjusted to get a better fit using values of $\eta_m = 1.6\%$, $\eta_{E_1} = 0.3\%$, η_{E_2} and $\eta_{G_{12}} = 0.7\%$. Although these values gives damping in good agreement with the experimental values they are not very physical since a glass fibre filament is isotropic and the corresponding damping should therefore also be isotropic [4].

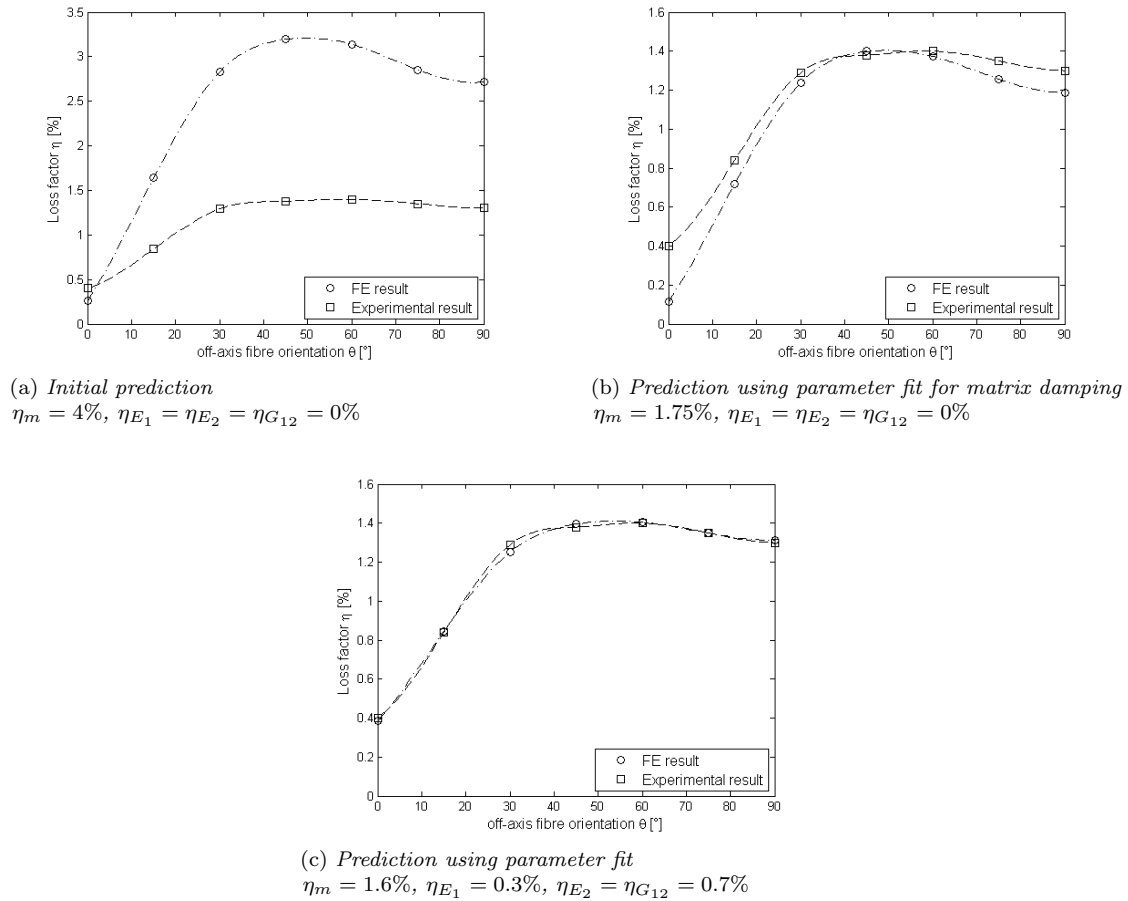
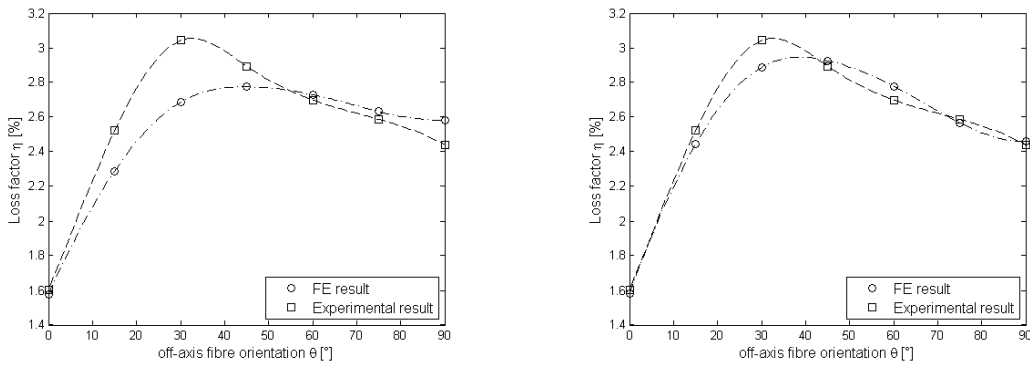


Figure 15: Correlation between numerical damping predictions and experimental results for the glass fibre.

Figure 16a shows the corresponding fit for the Kevlar[®] fibre beam where damping values of $\eta_m = 3.3\%$ and $\eta_{E_1} = \eta_{E_2} = \eta_{G_{12}} = 1.5\%$ has been used. In general there is good correlation for both 0° and 90° orientations but the high damping in the 30° orientation found in the experiment is not resolved by the numerical model. The high loss factor at 30° is due to the bending-twisting stress coupling term C_{16} . An off-axis laminate is both unbalanced and unsymmetric which makes the stress coupling significant. In [8] it is stated that the loss factor increases proportionally to the bending-twisting coupling and the that effect is most apparent around 30° fibre orientation which also can be seen in Figure 17b. When comparing the experimental results for the glass and Kevlar[®]

fibre it is clear that the effect is more pronounced in the Kevlar[®] beam. This is most likely due to the worse bond between fibre and matrix in the Kevlar[®] case, which as mentioned in Section 2.2.1 has a large influence on the damping in shear deformation. This worse bond can be attributed to the absence of good coupling agents for Kevlar[®] fibers [4]. The twisting in the bending mode at 30° fibre orientation for the Kevlar[®] fibre can be seen in Figure 17a. For extensional vibrations where there is no bending-twisting coupling the maximum damping can instead be found at 45° where the maximum in-plane shear occur [14]. The extra damping introduced by the interphase can be simulated using the numerical model by introducing a higher fibre damping specifically in shear. The results for damping values of $\eta_m = 0.033$, $\eta_{E_1} = 1.5\%$, $\eta_{E_2} = 1.2\%$ and $\eta_{G_{12}} = 3.3\%$ can be seen in Figure 16b. In comparison with Figure 16a there is clearly a better fit.

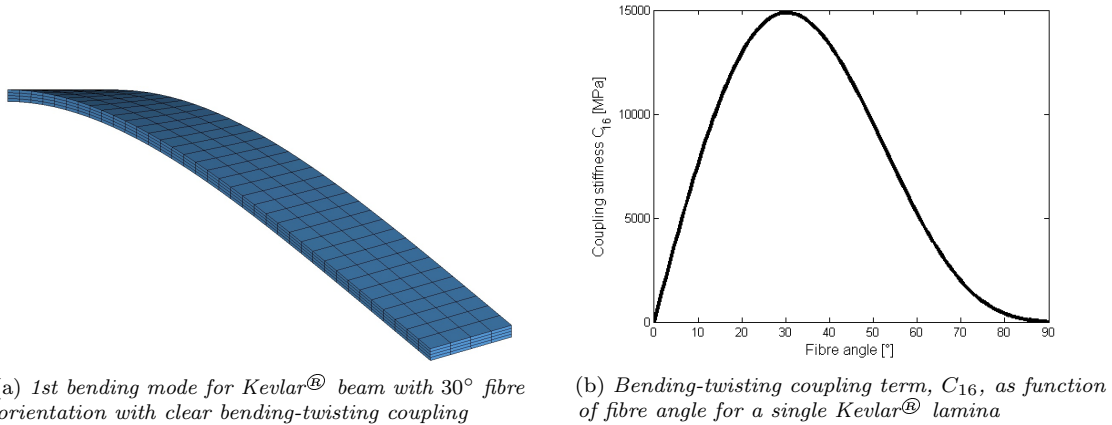
Although the intent of the micromechanical model was to predict the damping in CFRE it is clearly able to predict the damping of both glass and Kevlar[®] composites through adjustment of the four material damping parameters η_m , η_{E_1} , η_{E_2} and $\eta_{G_{12}}$.



(a) Initial prediction
 $\eta_m = 3.3\%$ $\eta_{E_1} = \eta_{E_2} = \eta_{G_{12}} = 1.5\%$

(b) Prediction using parameter fit
 $\eta_m = 0.033$ $\eta_{E_1} = 1.5\%$ $\eta_{E_2} = 1.2\%$ $\eta_{G_{12}} = 3.3\%$

Figure 16: Correlation between numerical damping predictions and experimental results for the Kevlar[®] fibre.



(a) 1st bending mode for Kevlar[®] beam with 30° fibre orientation with clear bending-twisting coupling

(b) Bending-twisting coupling term, C_{16} , as function of fibre angle for a single Kevlar[®] lamina

Figure 17: Bending-twisting coupling C_{16} .

2.3 Foam core damping

Material data for the Rohacell[®] Polymethacrylimide (PMI) foam core used as the sandwich core can be found in [29]. Unfortunately there is no available data on the dynamic stiffness from the manufacturer. However, DMTA was performed on the core material in [19]. The resulting damping found from that analysis can be seen in Figures 18 and 19. There is a large scatter in the measured data for each individual test specimen but also a $\sim 15\%$ difference between the two samples tested. This indicates that the foam damping is difficult to measure and that the DMTA technique is sensitive to the specimen set-up.

Assuming an average of the values from the two tests, the loss factor of the foam is set as $\eta \approx 2.5\%$.

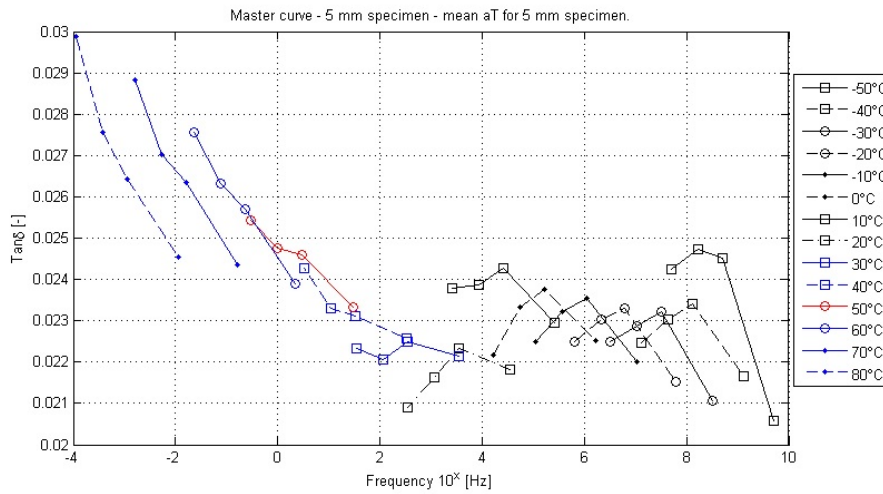


Figure 18: *Master curve of loss tangent, $\tan(\delta)$, for the 5 mm specimen*

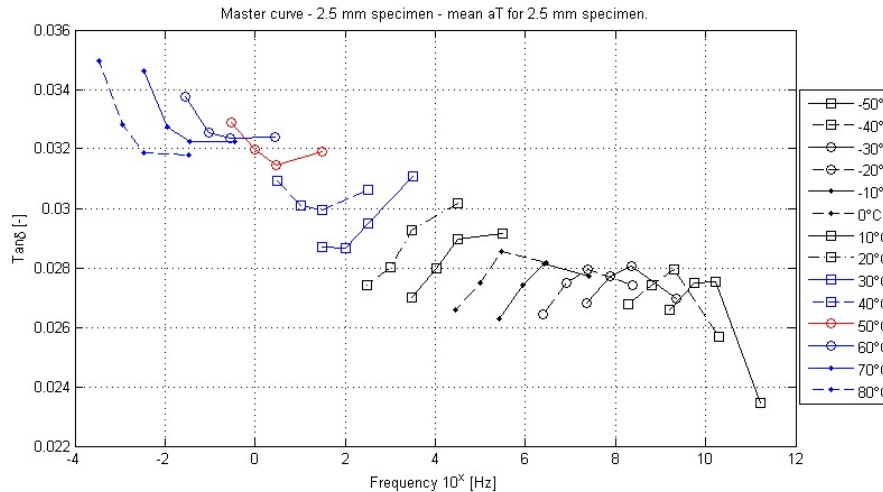


Figure 19: *Master curve of loss tangent, $\tan(\delta)$, for the 2.5 mm specimen*

3 Experimental testing

3.1 Test design

3.1.1 Specimen design

The aim with the experimental testing was to validate the predicted orthotropic damping properties of the composite as well as the HCF capability of the foam core. The complex geometry of the existing composite OGV concept with its curvature and varying thickness creates eigenmodes with complex shapes even for low mode numbers as seen in Figure 20. As a consequence it would have been difficult to design a test set-up were the individual properties of the composite and the core could be evaluated easily using this geometry. Therefore a simplified geometry had to be designed, with which the predictions of the damping and the fatigue properties could be validated. The simplest geometry where this could be achieved was a sandwich beam. As mentioned in Section 1.4 the test pieces were manufactured by ACAB and limitations in tooling allowed for only flat geometries with a maximum dimension of 350x300x20 mm. Due to cost and time limitations only one of these plates could be manufactured. This meant that the test pieces needed for all test had to be extracted from this plate.

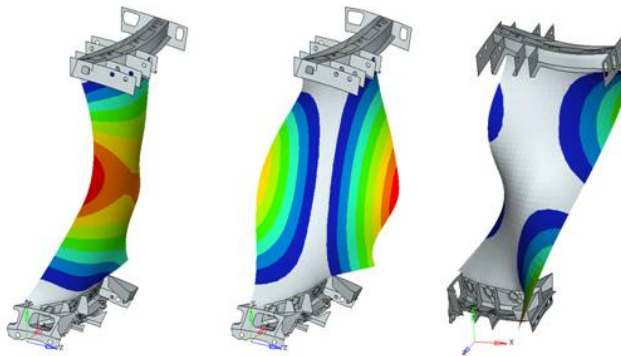


Figure 20: *First eigenmodes of OGV.*

For the HCF test the beam had to be designed in a way to ensure that fatigue failure would occur in the core and not in the faces. The total deformation of a beam consists of both bending and shear deformation. The bending deformation depends on the flexural rigidity, D , which for a sandwich beam with equal faces is given by [33]

$$D = \int Ez^2 dz \approx \frac{E_f t_f d^2}{2} \quad (34)$$

The shear deformation, in turn, depends on the shear stiffness, S , which is given by

$$S \approx \frac{G_c d^2}{t_c} \quad (35)$$

The different thicknesses and moduli of the sandwich cross-section can be seen in Figure 21. In both expressions, (34) and (35), it has been assumed that the faces are thin $t_f \ll t_c$, the faces have high shear stiffness, G_f , and the core is weak $E_c \ll E_f$.

The ratio of shear to bending deformation depends on the shear factor, ϕ , which is given by

$$\phi = \frac{D}{L^2 S} \quad (36)$$

where L is the length of the beam. It is clear from Eq. (34) that the bending stiffness is mostly depending on the in-plane face stiffness, E_f , and beam thickness, d , while the shear stiffness on the

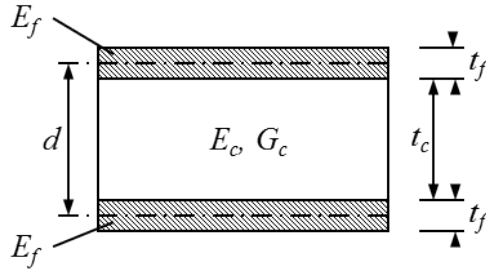


Figure 21: *The thicknesses and moduli through the beam cross-section.*

other hand is mostly dependent on the core stiffness, G_c , and thickness, t_c . This means that the core mainly experience shear deformation while the faces experience in-plane tensile deformation. Thus, to achieve the goal of fatigue in the core for a certain mode of deformation it must be assured that the shear in the core is higher than the strain in the faces in relation to their individual fatigue strengths.

The HCF test is made at the eigenfrequency of the test piece which means that there will be a $R = -1$ stress ratio loading condition. The test pieces will be run in a range of 10^6 to 10^8 load cycles and therefore the static material strengths has to be scaled accordingly. The shear stress life of the Rohacell[®] WF51 foam, which is a lower density version of the foam core used at GKN, has been covered in [33] and shows the behaviour seen in Figure 22. In [19] it was shown that the fatigue data between the two foams correlate well, as seen in Figure 23, and that the maximum shear strength at 10^8 load cycles can therefore be set as

$$\tau_{10^8} = 0.3\hat{\tau} = 1.5 \text{ MPa} \quad (37)$$

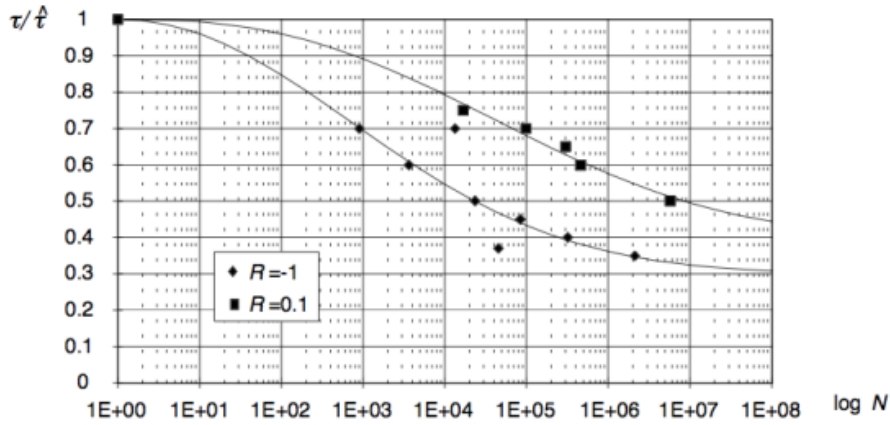


Figure 22: *S/N-curve for Rohacell[®] WF51 foam, from [33].*

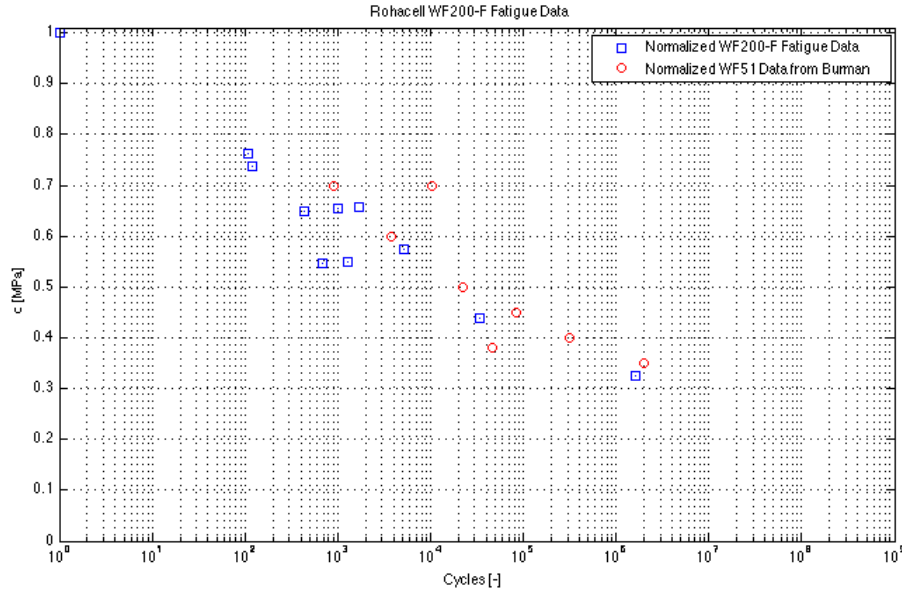


Figure 23: S/N -data correlation for the two Rohacell[®] foams, from [19].

The fatigue properties of the CFRE is covered in [28]. The report present experimental strain life data for 0° and 45° dominated laminates as well as for a Quasi-Isotropic laminate. The 45° dominated lay-up show the lowest fatigue limit of the three and was therefore used as a conservative limit during design. Only experimental results for load cycles between 10^3 and 10^6 were available and therefore a log-linear extrapolation was made up to 10^8 load cycles with the assumption that there is no fatigue limit associated with the material.

The fatigue strength ratio of elastic strain in the CFRE to the shear stress in the core, ϵ_1/τ_{xz} , as a function of load cycles, N , can be seen in figure 24. Since the CFRE is assumed to have no fatigue limit while the core has such a limit it is for the most extreme value, 10^8 load cycles, where the most critical value can be found. This means that a strength ratio of

$$\frac{\epsilon_1}{\tau_{xz}} < 0.08 \text{ MPa}^{-1} \quad (38)$$

is needed during the test to ensure fatigue failure in the core for up to 10^8 load cycles.

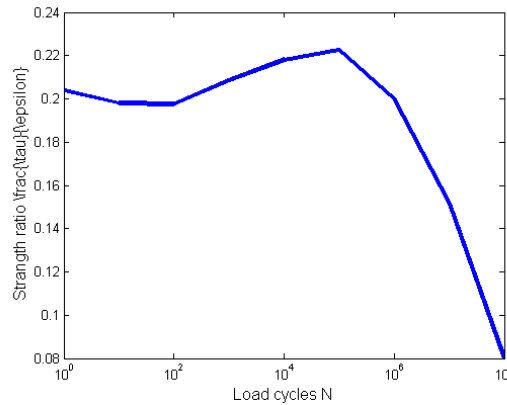


Figure 24: The variation of the fatigue strength ratio, $\frac{\epsilon_1}{\tau_{xz}}$, with increasing number of load cycles.

To get an indication of the actual strength ratio in a sandwich beam during different modes of vibration a modal analysis was performed in ANSYS®. A beam with length $L = 200\text{mm}$, width $w = 20\text{mm}$, core thickness $t_c = 6\text{ mm}$ and face thickness $t_f = 2\text{ mm}$ was modelled in a hinged condition. The FE-model can be seen in Figure 25. The beam was modelled using the solid shell element SOLSH190 for the skin and the solid element SOLID185 for the core. Both these element types was shown to be suitable when modelling sandwich structures in [22]. The hinged boundary condition was modelled using CERIG elements connecting all nodes on the end surface of the beam to an independent single node at the center of the beam's cross-section with only rotational DOFs. Constraining the model in this way showed the best correlation with the analytical solution using sandwich theory. The composite was in this initial stage modelled as Quasi-Isotropic using material data from [28] before the effects of laminate lay-up had been investigated.

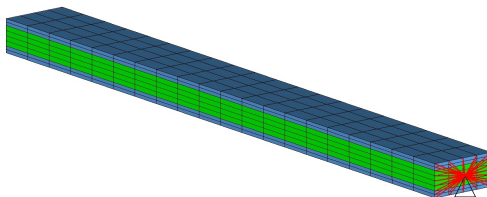


Figure 25: *FE-model of hinged sandwich beam*

The first three bending modes and corresponding eigenfrequencies from the analysis can be seen in Figure 26 and Table 2 respectively. The contour plot in the figures show the amount of transverse shear stress, τ_{xz} , in the core. The absolute value of the stress is not of interest in these figures since the mode shapes are scaled to the mass of the system during the analysis which gives unphysical deformation amplitudes. However, the distribution of the stress along the beam and its magnitude in relation to the strain in the faces, ϵ_1 , is of interest. The shear deformation of the core in the first eigenmode seen in Figure 26a is not suitable in a test perspective since the maxima are located near the edges of the beam. Since the mode is symmetric it means that it has the same maximum on the other edge of the beam. This will make it heavily dependent on exactly how the beam is supported and therefore difficult to predict. The second eigenmode, in Figure 26b, is better in this aspect since it has the maximum located in the center. It is also beneficial that there is only one maximum which means that it can be assured that the failure will occur in this area. One disadvantage of the second eigenmode compared to the first is the clearly higher frequency. The shaker used as exciter in the HCF test has a limited acceleration and force which means that the frequency will have to be kept within reasonable limits. Also the third eigenmode, seen in Figure 26c, could be used but again with the disadvantage of two maximum points and an even higher frequency. The ratio of shear to bending deformation increases with higher eigenmodes which is evident by the decrease in strength ratio seen in Table 2. This is logical since an increase in eigenmode can be seen as a shortening of the beam length which is one of the factors affecting the shear factor in Eq. (36) [33]. Given these results it was decided that the second mode is of highest interest and should be further investigated.

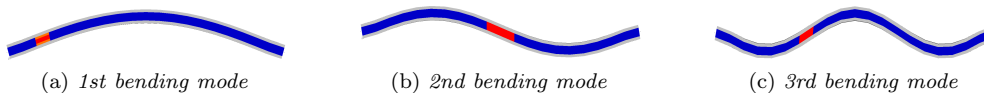


Figure 26: *Mode shapes of hinged beam*

The analytical equation for the eigenfrequencies of a simply supported beam is given by [33]

$$\omega = \frac{m^2 \pi^2}{L^2} \sqrt{\frac{D}{\rho^* (1 + m^2 \pi^2 \phi)}} \quad (39)$$

where m is the mode number. Using this equation on the beam gave the analytical frequencies seen in Table 2. The difference between the FE solution and the analytical solution originates from the

Table 2: Correlation between FEA and analytical equation for sandwich beam with 2mm face thickness and 6mm core thickness

Mode	1st	2nd	3rd
FEA [Hz]	672	1943	3339
Analytical [Hz]	657	1805	2961
Difference [%]	2.3	7.6	12.8
Strength ratio [MPa ⁻¹]	0.081	0.057	0.022

assumption of thin faces $t_f \ll t_c$ in the analytical equation which neglects the bending stiffness of the faces around their own central axis. This assumption is said to be valid for $\frac{t_c}{t_f} > 5.77$ which is not true for the current beam dimensions were $t_c/t_f = 3$.

Performing the same analysis for a sandwich beam with a 25mm core and 1mm faces for which the analytical equation is valid gave the results shown in Table 3. Better agreement is achieved in this case and the results also show that the applied constraint using CERIG elements simulate the hinged condition well.

Table 3: Correlation between FEA and analytical equation for sandwich beam with 1mm face thickness and 25mm core thickness

Mode	1st	2nd	3rd
FEA [Hz]	1216	3021	4803
Analytical [Hz]	1217	2983	4698
Difference [%]	0.1	1.3	2.2

The eigenfrequency of a beam is highly dependent on how it is constrained. Therefore a comparison of different support types was performed to find the most suitable support for the test set-up. The second bending mode shape for different support type combinations can be seen in Figure 27 (third bending mode in Figure 27a). The corresponding eigenfrequencies are listed in Table 4 where it is clear that the eigenfrequency increases with increased amount of imposed constraints which was expected.

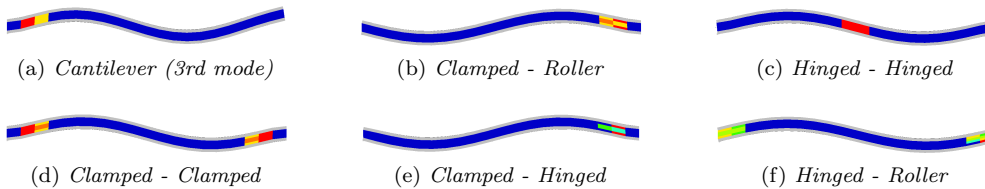


Figure 27: Different support types influence on mode shape and core shear stress

It is clear from Figure 27 that the hinged condition is the most suitable in regard to the transverse shear stress distribution in the core since it is the only one with the global maxima in the middle of the beam. The stiffening effects from the other types of support causes a maximum in stress towards the edge of the beam which is unwanted. Using symmetric supports is beneficial since the mode shape will be perfectly unsymmetric around the midpoint for easier predictability.

To make the beam more easily fixated and robust it was decided to make its ends out of solid CFRE. This also meant that a drop-off transition was needed in the interface between the solid edges and the core to avoid local failure in this region during loading. The effect of the solid edges on frequency and mode shape was initially analysed using a model without a transition region seen in Figure 28 where the solid edge has a length of 40 mm. The results from the modal analysis can be seen in Table 5. A stiffness increase can be seen for all modes when comparing to Table 2 but to a smaller extent for the second mode. While the strength ratio for the first and third mode get worse the addition of the solid edge is actually beneficial for the second mode which gets a better mode shape.

The HCF test should test the fatigue capability of the foam core at frequencies near the first

Table 4: Comparison of eigenfrequencies for different support types

Support type	Cantilever (3rd mode)	Clamped - Roller	Hinged - Hinged
Frequency [Hz]	2469	2004	1943
Support type	Clamped	Clamped - Hinged	Hinged - Roller
Frequency [Hz]	2139	2021	1842

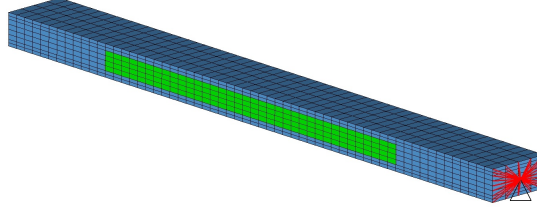


Figure 28: *FE-model of hinged sandwich beam with solid edges*

Table 5: Comparison of eigenfrequencies between FE-models with and without solid edge.

Mode	1st	2nd	3rd
Homogenous [Hz]	672	1943	3339
Solid edge [Hz]	998	2005	3572
Strength ratio [MPa ⁻¹]	0.118	0.044	0.032

eigenmodes of the OGV. 2005Hz is well above this frequency which means that the eigenfrequency of the beam has to somehow be lowered. In addition to this aspect the hydraulic shaker at GKN, used for the HCF test, has performance limited to:

- Maximum frequency: 3kHz
- Maximum acceleration: 120g
- Maximum displacement: 25.4mm
- Maximum force Sine wave: 13.3kN
- Maximum force random: 12kN

Equation (37) sets a required stress level needed in the core during the HCF test to achieve failure. To reach this amount of transverse shear stress in the second eigenmode for the hinged beam a displacement amplitude, A , of $\sim 0.3\text{mm}$ is needed. The maximum acceleration for a harmonic oscillation at this amplitude and frequency, 2005Hz, is

$$a_{max} = \max \left(A \frac{d^2 \sin(\omega t)}{dt^2} \right) = A(2\pi f)^2 \approx 4850g \quad (40)$$

This acceleration is way higher than the capability of the shaker and means that the beam would need to have a vibration magnification factor of around ~ 38 at the second eigenmode for the shaker to be able to drive the motion. This is not very probable given that an ideal magnification factor of 40 can be expected for a SDOF system with a loss factor of 2.5% as the core. This means that the eigenfrequency of the beam has to be lowered. Looking at the analytical equation (39) together with Eq. (34) and (35) it is possible to see which parameters affect the eigenfrequency. Each parameter's influence on the eigenfrequency can be seen in Figure 29.

Reducing the core thickness or face thickness is clearly not an effective way of lowering the frequency. A reduction in core thickness would also cause a drop in the shear factor which is unwanted. Reducing the face thickness is also not a good option since the test specimen should also be used to determine the damping in the CFRE. With increasing volume ratio of foam compared to CFRE it will be harder to discern the damping associated with the CFRE. By changing the laminate lay-up in the faces its effective modulus, E_f , can be adjusted. Reducing the modulus is however, in this specific case, not a good idea since this simultaneously reduces the shear factor.

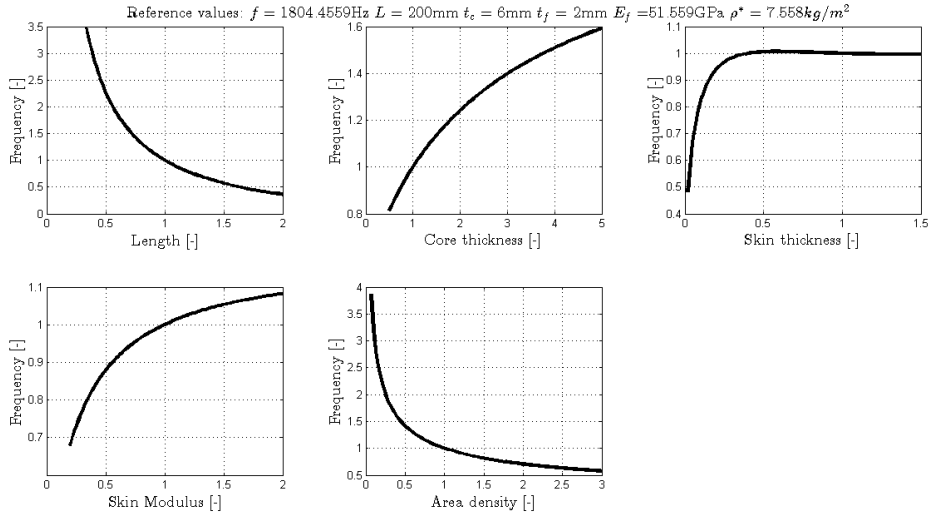


Figure 29: *Parameters effect on beam eigenfrequency.*

The same argument is true for the length of the beam since both eigenfrequency and shear factor is proportional to $1/L^2$. The only remaining option is then to increase the surface density, ρ^* , i.e., the mass of the system. Looking at Figure 29, the mass has a large influence on the eigenfrequency and could be an effective way in lowering the frequency. The mass however, has to be added to the system without introducing damping or affecting the mode shapes in an unwanted way. One identified solution to this problem was to add the mass as rotational inertia at the hinged points of the beam. This means that the eigenfrequency can be tuned without changing the geometry of the beam. However, the added inertia introduces bending moments around the beam's ends which causes a change in mode shape which has to be accounted for.

The effect of adding mass for increased rotational inertia was tested by adding an inertia of $3 \cdot 10^{-4} \text{kgm}^2$ at both hinged ends of the beam. This inertia is equivalent to the inertia of a steel cube with a side length of $\sim 47 \text{mm}$ around one of its principle axes. The added inertia lowered the second eigenfrequency from 2005 Hz to 372 Hz which is in the region of the first bending mode of the OGV. At this frequency the maximum acceleration is only 167 g which means that it will be much easier for the shaker to drive the motion. However, the added inertia has increased the bending in the mode shape and has due to that worsened the strength ratio to 0.079megaPa^{-1} which is at the limit in Eq. (38). The thickness of the beam should therefore be increased to get a better strength ratio. Going from a 10 mm to a 12 mm thick sandwich would also be beneficial regarding manufacturing since a tool for making 12mm laminates was already available at ACAB. Using another thickness would increase cost and manufacturing time. Increasing the total thickness to 12 mm by increasing the core thickness to 7 mm and the face thickness to 2.5mm kept a similar thickness ratio of 2.8 compared to the original 3 for the 10 mm sandwich. Performing the same modal analysis with the added inertia for the 12 mm beam gave an eigenfrequency of 459 Hz and a strength ratio of 0.068MPa^{-1} . These two numbers were deemed sufficient and the dimensions of the faces and the core were set accordingly. As a final modification the beam length was increased to 230 mm and a 9 mm hole was added to each end to facilitate easier fixation of the beam while still maintaining an effective length of 200 mm between the hinge support points.

The overall dimensions of the beam were set using a relatively simple model with homogenised QI faces. A more detailed model was needed for the design of laminate lay-up in the faces. The conventional way of modelling CFRE with commercial FE-software is to use layered elements where multiple plies can be modelled in a single element with reduced computational cost. In this case however the drop-off schedule should be modelled explicitly which means that every ply has to be modelled individually, i.e., one element per ply. A rule of thumb in the aerospace industry is to keep a minimum of 1:10 ratio between ply thickness and ply drop-off [22]. Since each ply is 0.25 mm this means that it should be a minimum of 2.5 mm between each drop off. To keep the

number of elements in the analysis to a minimum the solid shell element SOLSH190 was used for both faces and core which allows for a larger aspect ratio compared to regular solid elements. The element length was set to 1.25 mm in the length direction of the beam to achieve some detail in the drop-off area. The element thickness was set to 0.25 mm in accordance with the ply thickness. The element width was set to 2.5 mm to get enough resolution to identify twisting modes and bending-twisting coupling. The FE-model can be seen in Figure 30. A 30 mm clamped area was assumed needed for proper mounting of each end of the beam in the fixture and was simulated using a CERIG connection from the hinged point to the nodes on the upper and lower surfaces.

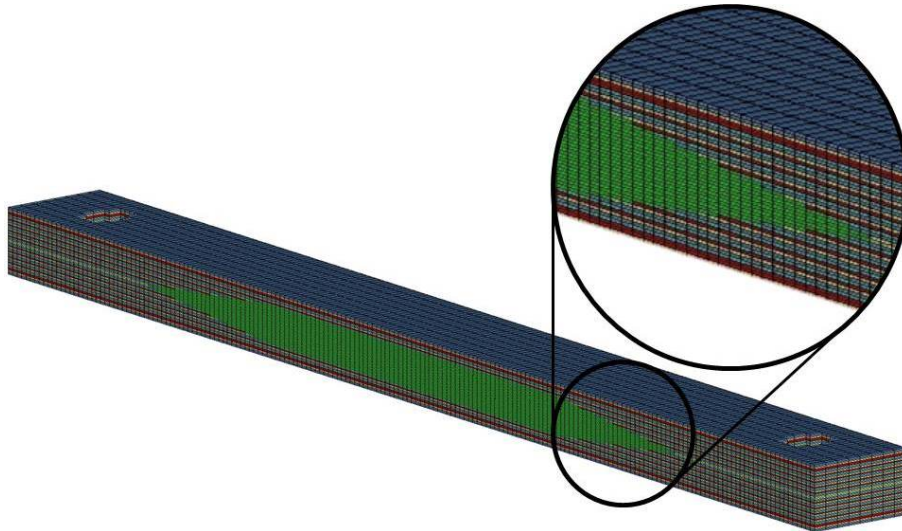


Figure 30: *Detailed FE-model*

It was decided to let the 24 plies in the solid CFRE edges have a QI lay-up of $[0^\circ/+45^\circ/90^\circ/-45^\circ]_n$. Only a rotation of $\pm 45^\circ$ between adjacent plies was allowed to minimise the difference in stiffness and the risk of delamination. Two different lay-up schedules for the faces was evaluated and can be seen in Table 6. As many $\pm 45^\circ/90^\circ$ plies as possible was wanted since these orientations introduce more matrix dependent deformation, and therefore damping, compared to the 0° -ply. However, a $\pm 45^\circ/90^\circ$ dominated laminate is not as stiff and the first lay-up in Table 6, which is $\pm 45^\circ$ dominated, does not pass the strength ratio requirement. The second lay-up with two 0° -plies in the outer layer on the other hand passes this requirement and was chosen as the final lay-up. This lay-up is both balanced and symmetrical, hence the so called coupling stiffness matrix, B , will be zero and there are no bending-extension coupling at the same time as the bending-twisting coupling is kept small. From Figure 31 it is clear that the maximum transverse shear stress using this lay-up is still concentrated to the centre of the beam as expected. Also no stress concentrations in the drop-off region are visible which means that one can be confident that the core will fail at the centre as intended.

Some strain concentrations at the transition point where the beam is constrained is apparent in Figure 32. However, the way the constraint has been modelled is not very physical and in real life there will be some relative motion between the beam and fixture which will release these strains. Instead the strain of interest is located at the point of maximum curvature where the faces experience pure tensile strain due to bending. It was the strain found here that was used in the calculation of the strength ratio in Table 6.

Table 6: Comparison of face lay-up:s

	Frequency f [Hz]	Strength ratio ϵ_1/τ_{xz} [MPa $^{-1}$]
$[0/+45/+45/90/-45/-45/0/+45/90/-45]$	418	0.095
$[0/0/+45/90/90/-45/0/+45/90/-45]$	459	0.067

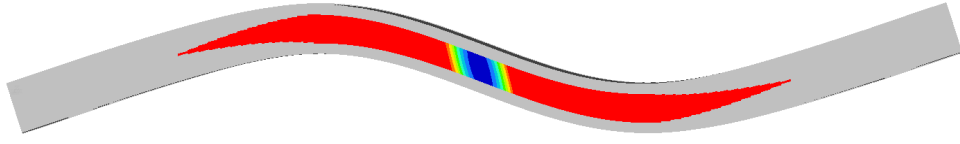


Figure 31: *Transverse shear stress maximum in core*

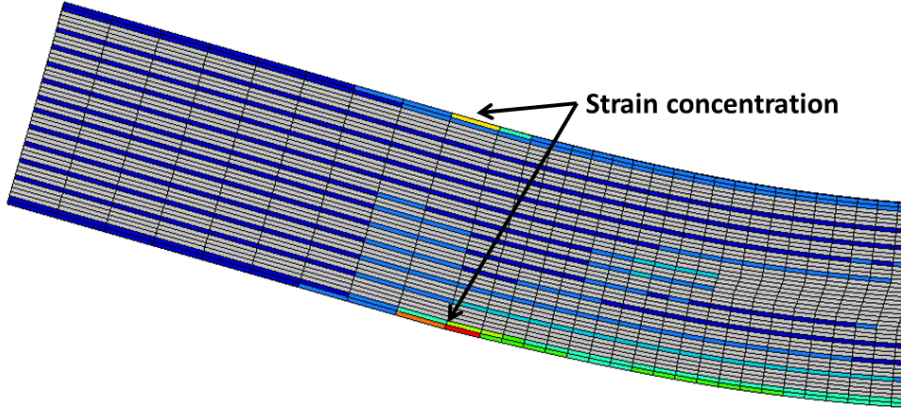


Figure 32: *First principal strain in 0° plies.*

With the dimensions of the beam set and the lay-up in the faces decided, the design of the sandwich beam was completed. The final manufacturing specification of the beam can be found in Appendix A.

3.1.2 Fixture design

The beam was designed to be tested in its second bending mode. Since this is an unsymmetric mode the beam has to be excited unsymmetrically using two excitation sources 180° out of phase to trigger the mode. This set-up was not possible in this case since only one shaker was available at GKN. The remaining option was to excite the beam using the type of set-up shown in Figure 33. With this type of set-up the deformed shape consist of a superposition of the second eigenmode and the deformation caused by the exciter. Solving the inhomogeneous boundary condition problem in Figure 33 analytically for an isotropic beam gives the following equation for the beams deflection at equilibrium

$$u(x, t) = \sum_{n=1}^{\infty} (\phi_n(x)(A_n \sin(\Omega t))) + \hat{u} \sin\left(\frac{\pi x}{2L}\right) \sin(\Omega t) \quad (41)$$

$\phi_n(x)$ is the mode shape of mode n , A_n and b_n are functions depending on the boundary conditions, Ω is the excitation frequency and \hat{u} is the excitation amplitude. The deformed shape when the excitation frequency is close to the second eigenfrequency can be seen in Figure 34. Because of the high magnification factor, A_2 , close to the eigenfrequency the deformed shape mainly consist of the contribution from the eigenmode.

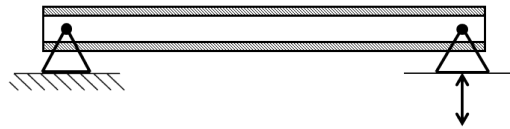


Figure 33: *Principal sketch of the HCF test set-up*

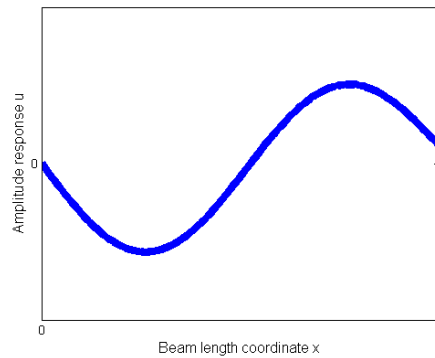


Figure 34: *Analytical solution of beam deflection at equilibrium*

The shaker used for the HCF test can be seen in Figure 35. The top of the shaker head, which is the excitation source, and the static table has been indicated. These are the two corresponding supports in the schematic set-up in Figure 33.

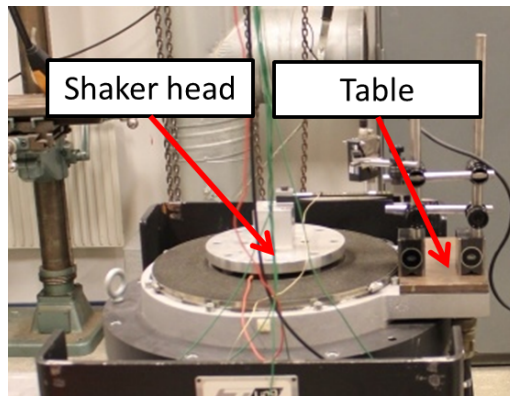


Figure 35: *The hydraulic shaker used for the HCF test.*

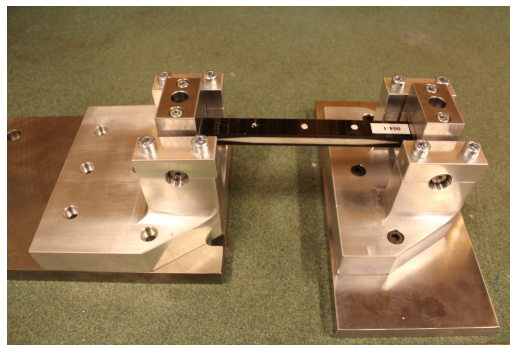


Figure 36: *HCF fixture with attached test specimen.*

The final fixture design can be seen in Figure 36. The part of the fixture to the left is the one mounted on the shaker head. This part had to be designed with mountings and shape that were as evenly distributed as possible to minimise the out-of-balance forces on the hydraulic cylinder during excitations. The forces the fixture experience during the shake test are relatively minor and did not pose any constraint on the design. However, the fixture had to be made stiff enough not to introduce any unwanted flexure or damping in the system, and at the same time it had to be made as light as possible to minimise the load on the shaker. Therefore the fixture was made mainly out of aluminium whereas steel was used for the pieces requiring high rotational inertia. The base for

the two supports was made out of a single piece of aluminium for increased linearity between the two hinges and for easier manufacturing. Unfortunately, the shaker head and the fixed table of the shaker are not aligned vertically which resulted in that an adapter plate, seen underneath the fixture to the right in Figure 36, had to be manufactured and added.

To come as close as possible to the ideal hinged condition in the actual fixture, bearings were used in form of brass bushings. The use of roller bearings was not recommended given their uncertain performance in this type of application with high oscillations and small rotations [10].

The fixation of the beam was made easily dismantlable to facilitate the change of test specimens between tests but also for the possibility to alter the rotary inertia of the system easily.

Modal analysis of an early design of the fixture and beam assembly showed that the eigenfrequencies of the fixture lies well above the frequencies of interest for the HCF test. The three lowest eigenmodes of the fixture and beam assembly can be seen in Appendix C. This ensured that the fixture itself should not influence the measurements or results.

An exploded view of the fixture assembly can be found in Appendix B.

3.2 Manufacturing

The test pieces were manufactured at ACAB in Linköping using a RTM process. The different stages during manufacturing can be seen in Figure 37. Initially, the laminae in the lower part were cut and placed and then precompacted. The foam core was then machined to net shape using a mill and placed in the preform. The lamina in the top part was then cut and placed and the complete sandwich was precompacted to 13mm thickness for easier handling and maintained fibre angle tolerances. The sandwich plate was then put in the 12mm RTM tool and placed in the RTM press and preheated to 120°C. The resin was preheated to 80°C and then infused using a pressure of 7 bar. Once the mould was completely filled the temperature was ramped up to 180°C and then cured for two hours as specified by Hexcel®. The mould was then slowly cold down before demounted from the press after which the plate was cut out of the tool. The beam specimens were then cut to their final shape using water jet cutting and the holes were drilled.

The complete beam specimens from the first plate can be seen in Figure 38. From this picture it is clear that the core has been severely deformed. The core had not been control measured before the infusion and the deformed core was believed to be caused by deficient pre-machining. Additionally, the plate was manufactured using the wrong fibre orientations were all plies were rotated 90° relative to the manufacturing specification. According to the analysis in Section 3.1.1 a beam with this lay-up has too low bending stiffness which would cause fatigue in the faces instead of the core. Therefore a second plate was made with the right orientation.

The final specimens from the second plate can be seen in Figure 39. By looking closely at the image it can be seen that the faces are slightly unsymmetric. The lower face is close to the wanted thickness of 2.5 mm while the upper face is closer to 3 mm. The thickness of the specimens were on average 11.91 mm which is slightly below the nominal value but is most probably caused by shrinkage after curing. The nominal dimensions of the core after milling had been checked and were within tolerance which means that the core had been compressed approximately 0.5 mm during curing. The amount of creep experienced by the core during curing depends on the cure time, temperature and pressure. The compressive creep of the Rohacell® HT-foam, which is the heat treated version of the regular foam, after 2h curing at 180°C is below 1% [30]. For the regular foam this value is 3%. Evonik states that the regular foam can be processed at up to 130°C. Since the curing temperature used in the RTM process was 180°C the temperature is the most probable reason for the creep/collapse of the core and the unsymmetric faces.

The weights of the specimens were on average 60.2g. This should be compared to the expected value of 62.3g from the FE-model using experimentally determined material data. The reason for this difference is not completely understood but may partly be explained by the manufactured beams having thickness and width which are slightly below the nominal value.

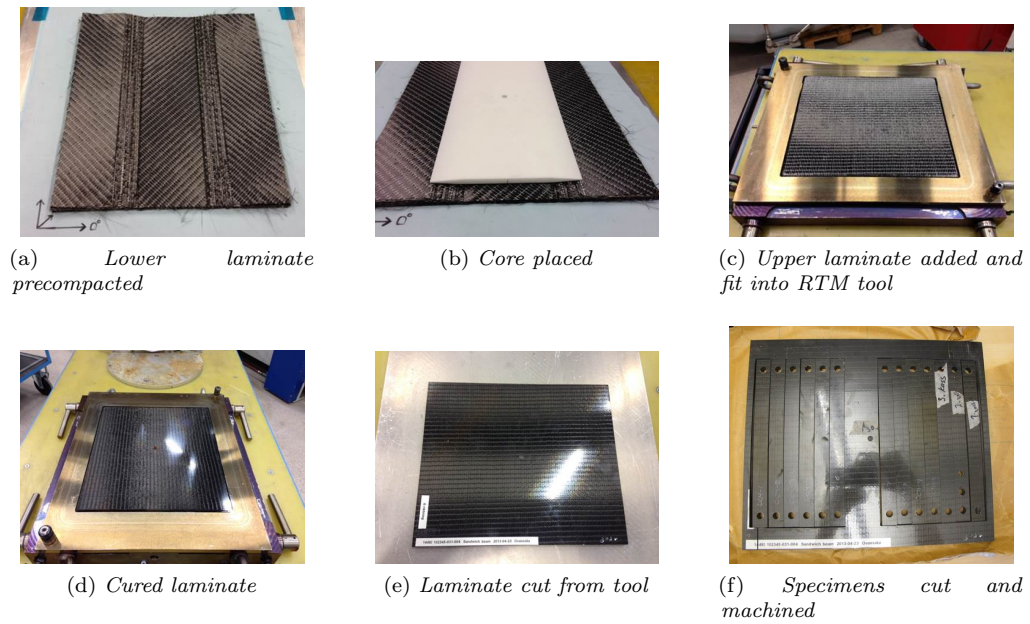


Figure 37: The different steps in the RTM manufacturing process of the beam specimens



Figure 38: Test specimens from first plate.



Figure 39: Test specimens from second plate.

3.3 Test execution

3.3.1 Ping test

The aim with the ping test was to identify eigenfrequencies and frequency response of the test specimens which will later on be used as reference when validating the FE-model used for prediction of the damping. A free-free ping test was performed to get reference values on eigenfrequencies and damping without the influence from a fixture affecting the results. The free-free ping test set-up can be seen in Figure 40a, where the ideal free-free condition is simulated using soft foam supports. The low eigenfrequency of the supports has minimal influence on the response in the relatively high frequencies of interest.

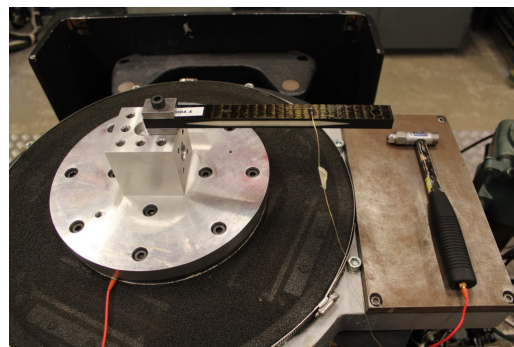
A ping test on a cantilever set-up was also made since the free-free condition cannot be modelled in a harmonic analysis in ANSYS®. The cantilever ping test set-up can be seen in Figure 40b. This is a simplified set-up of the so called Oberst Bar method which is a standardised test for measurement of dynamic moduli and damping. The specimen would ideally be clamped to an infinitely stiff support. This is not true in this case but the clamping of the specimens can be made consistent and the deviation from the ideal case can be approximated in upcoming FE-analyses. It was ensured that no eigenmode of the fixture coincided with those of the test specimen.

The accelerometer used for measuring the beam response was a 2250A-10 with a weight of 0.4 g excluding the cable. This is less than 1% of the weight of the test specimen. This small added weight has negligible effect on eigenfrequency, mode shapes and damping. The placement of the accelerometer was chosen as to have a good response for the three first bending modes, i.e., nodal lines were avoided. This made it possible to capture the response of all modes using only one ping test.

The impact was made using a PCB 086B01 piezoelectric hammer which acts as the input excitation signal in the system. The material used as the hammer tip effects the spectrum of frequencies excited during impact and has to be matched with the specimen such that all frequencies of interest are excited and as evenly as possible. In this case a regular metallic tip was sufficient. The mass of the hammer may also have to be adjusted so enough energy is entering the system to be able to detect the response. This was not an issue in the current case given the low weight of the test specimen. As for the accelerometer, the hammer strikes had to be positioned at a point where all modes of interest were excited. One such point was found at the very end of the specimen.



(a) *Free-free*



(b) *Cantilever*

Figure 40: *Ping test set-up*

The hammer and accelerometer was connected to a LDS Dactron Photon II signal analyser. The signal from the analyser was fed to a PC and processed using RT Pro Photon 6.21. The software records the time signal from both hammer and accelerometer with a 42kHz sampling frequency and 24-bit resolution and computes the Fourier Fast Transform (FFT) using a maximum of 8192 samples in real-time. The software was set to calculate the FFT using the average of five impacts for improved Signal-to-Noise Ratio (SNR). Since an average was made the so-called coherence, which is a measure of the relation between input and output signal, could be used as a measure of the quality of the signal. The coherence, C_{xy} , will always be $0 \leq C_{xy} \leq 1$ and therefore gives

Table 7: Experimental results for the free-free set-up.

Mode	1st	2nd	3rd
Frequency [Hz]	1355	2915	4501
Loss factor [%]	0.76	1.85	1.94

Table 8: Experimental results for the cantilever set-up.

Mode	1st	2nd	3rd
Frequency [Hz]	241	1434	3408
Loss factor [%]	1.21	1.30	1.94

the fraction of the output signal that is produced by the input signal. Using the coherence it was possible to ensure good positioning of the accelerometer and consistent hammer strikes. The coherence for one of the averaged ping tests can be seen in the top part of Figure 41. The coherence is good with values close to 1 for all frequencies except for some dips at anti-resonances.

The Frequency Response Function (FRF) calculated, which can be seen in the lower part of figure 40, is the so called inertance or accelerance which is the ratio of the acceleration response to the applied force excitation.

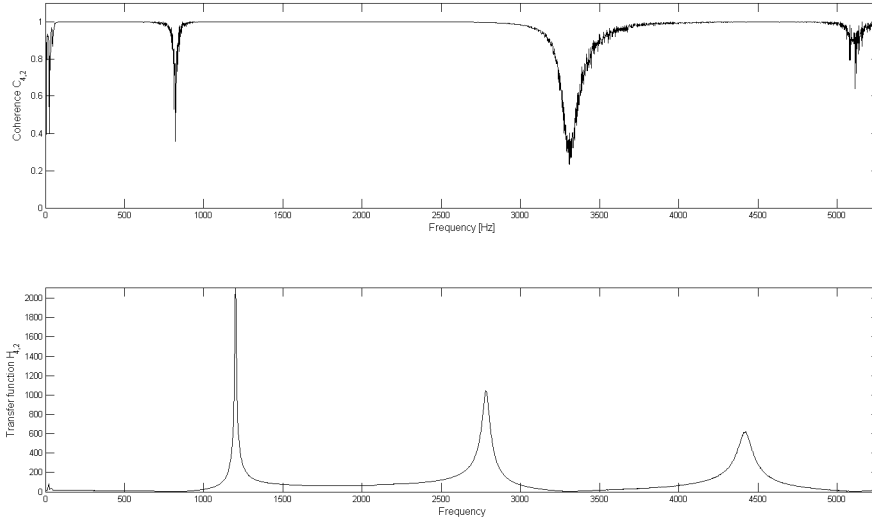


Figure 41: *Coherence (top) and transfer function (bottom) for free-free ping test.*

The frequency resolution in the FRF is not an issue when determining the eigenfrequencies from the peaks in this response curve. However, when calculating the damping through the half-power bandwidth method a high resolution is needed to capture the true shape of the response curve. This is especially true for low frequencies and low damping. A window function is always needed when performing the FFT of a finite signal. The choice of window function has a large influence on the shape of the FRF and therefore also the damping. In the software used there was no possibility to adjust the shape of the applied window function which meant that an apparent damping could be measured that is higher than the true value. For the cantilever set-up for example, a wrongly used exponential window function gave damping values for the first mode which was $\sim 2\%$ higher than the true value. For this reason a rectangular window was used which has minimal influence on the signal with the downside of a higher noise level. The issue with the frequency resolution had the implication that separate ping tests had to be made for each of the three eigenfrequencies in the cantilever set-up to get sufficient resolution. The frequencies and loss factors found for the cantilever and free-free set-up can be seen in Tables 7 and 8 respectively.

A trend of increasing damping with higher eigenmodes is apparent in both set-ups. There

is little difference in damping between the two set-ups which is an indication that the damping measured in the cantilever set-up originates from the material damping in the test specimen and not from external damping at the interface to the fixture.

The scatter in the measured results can be seen in Figures 42 and 43. Noting the scale on the axes there is a larger scatter in the damping data than the frequency data which shows that it is more difficult to get an accurate measurement of the damping. The larger scatter for the damping can also be an indication that there might be some slight differences between the test specimens that have a greater effect on damping than on the stiffness. The scatter in the cantilever data is in general larger which indicates that there might have been some slight differences between the set-ups of each specimen.

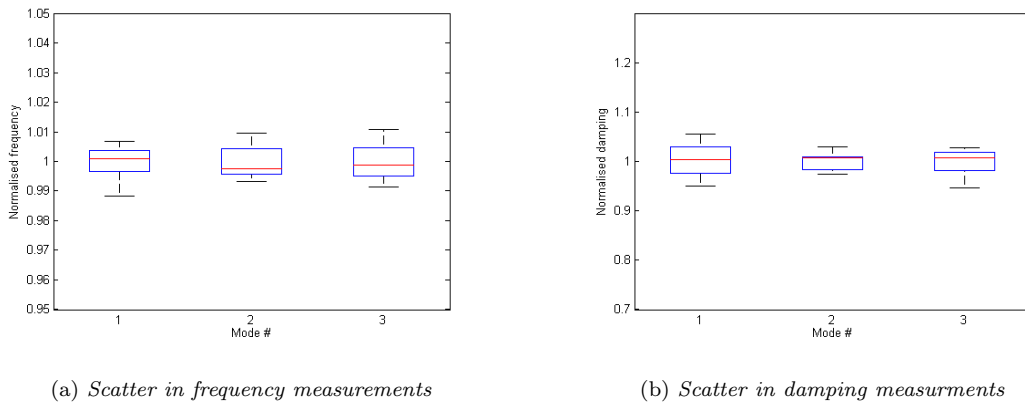


Figure 42: *Free-free*

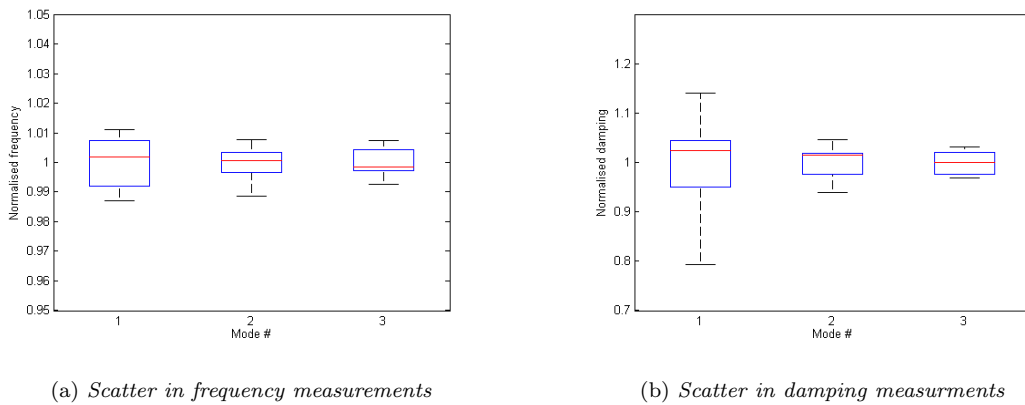


Figure 43: *Cantilever*

3.3.2 HCF test

The intent of the HCF test is to test the capability of the foam core in the frequency region of the first eigenfrequency of the OGV. Three accelerometers were attached at the positions of the white dots on the specimen in Figure 44 to measure the response and to coarsely capture the mode shapes. When performing a frequency sweep of the system up to the limit of the shaker at 3 kHz the second eigenfrequency was still out of range. Doing a ping test on the beam in the fixture showed that the eigenfrequency of the third bending mode could be found at 3250 Hz. This value is closer to the 3886 Hz found in ANSYS[®] for the beam with clamped ends than the 459 Hz found for the hinged ends. Changing to larger rotary masses and improving the lubrication of the bearings gave a minor

change in eigenfrequency indicating that the system is not entirely clamped. Doing a second ping test and hitting one of the rotary masses instead of the beam itself triggered the bending modes in the beam which also supports this fact. The non-functionality of the fixture is not completely understood but the most likely reason is the friction in the brass bearing which creates enough moment to resist all movement. With no time available to make any major modification on the fixture to lower the frequency to levels where the excitation amplitude needed for HCF could be reached, the current test set-up had to be abandoned.



Figure 44: *HCF fixture with attached test specimen.*

With the original set-up abandoned the most viable option was to further investigate the cantilever set-up since it is a common set-up and existing fixtures were already available. From the analysis in Section 3.1.1 and Figure 27a it was clear that the third eigenmode in the cantilever set-up could be of interest. Performing a modal analysis on the cantilever set-up with the detailed FE-model in Figure 30 gave the eigenfrequencies seen in Table 9 and the mode shapes seen in Figure 45. The second eigenmode showed a good shear stress distribution that was not located in the drop off region. The strength ratio satisfied the criterion in Eq. (38) and the frequency was in the working range of the shaker but still not low enough for it to be able to produce the amplitudes needed for HCF. The promising second eigenmode was tested in another modal analysis with an added mass on the edge of the beam. In the second eigenmode it is not the weight of the mass but rather its inertia that effects the frequency. By adding an inertia of $3 \cdot 10^{-4} \text{ kgm}^2$ in the modal analysis a frequency of 539 Hz was achieved. The mode shape can be seen in Figure 46 and when comparing to Figure 45b it is clear that the added inertia have had a large effect on the mode shape and has moved the point of maximum shear in the core closer to the centre of the beam. As a side-effect the added inertia has also worsened the strength ratio to 0.124 MPa^{-1} which is above the limit in Eq. (38). However, the limit value was set using the conservative value for the $\pm 45^\circ$ dominated lay-up from the reference. In this case, the highest tensile strain is experienced by a 0° -layer which has better fatigue properties and a strength ratio limit of 0.253 MPa^{-1} for 10^8 load cycles [32]. The modal analysis also showed that a beam deflection of $\sim 0.7 \text{ mm}$ is needed to reach the 1.5 MPa stress level needed for fatigue in the core, which should be in the range of the shaker. All these results indicate that this type of set-up should be possible to use for a HCF test.

Table 9: Eigenfrequencies and strength ratios for the cantilever FE-model

Mode	1st	2nd	3rd
Frequency [Hz]	246	1480	3010
Strength ratio [MPa^{-1}]	0.100	0.059	0.060



Figure 45: *Mode shapes of cantilever beam*

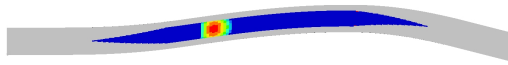


Figure 46: *Shear stress concentration in core for second eigenmode of cantilever set-up with added inertia at free end.*

The actual test set-up with the added weight can be seen in Figure 47. The high vibration amplitude and frequency at the second eigenfrequency caused accelerations in the region of 600 g which were on the limit of operation for the accelerometers used. Therefore the non-contacting laser vibrometer seen in the figure was used to measure the beam response instead.

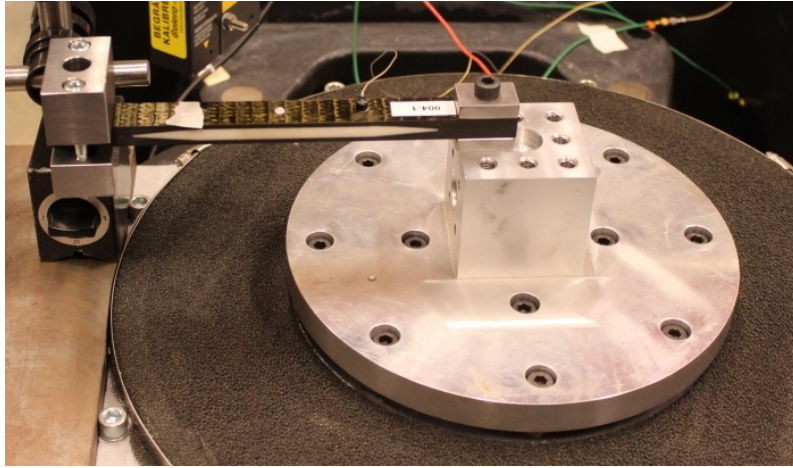


Figure 47: *HCF cantilever set-up.*

The shaker was set to perform an acceleration controlled vibration at 40 g which produced vibration amplitudes on the beam of $\sim 1.3\text{ mm}$. When identifying the second eigenfrequency during the initial frequency sweep it could be found at 450 Hz . After dwelling at the resonant frequency for less than one minute this frequency had drifted to 430 Hz . After $\sim 5 \cdot 10^5$ load cycles, the crack in the core seen in Figure 48 could be observed. After another $\sim 5 \cdot 10^5$ load cycles rapid changes in vibration amplitude could be observed and closer examination of the test specimen showed the large crack propagation seen in Figure 49.

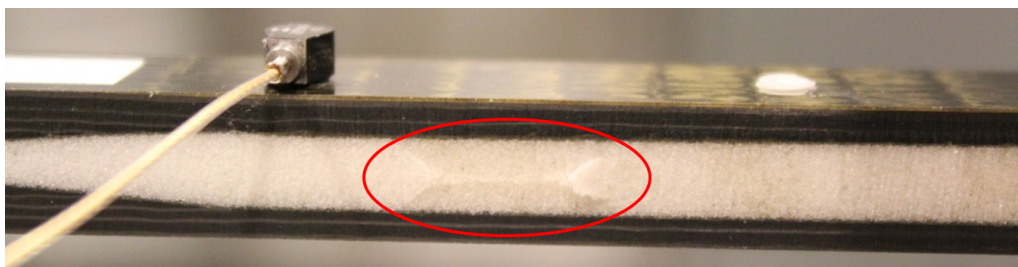


Figure 48: *Crack after $\sim 5 \cdot 10^5$ load cycles.*

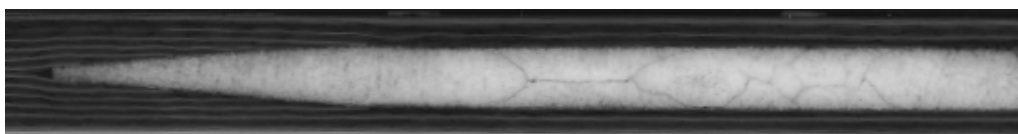


Figure 49: *Crack after $\sim 10^6$ load cycles.*

The shaker has a Resonance Search Track and Dwell (RST&D) functionality which means that it cannot only find the resonant frequency but also adjust the driving frequency to track the resonance

when there is a shift in frequency. A termination criterion can be set based on the amount of drift in frequency, the drift velocity and the change in resonance amplitude. A temperature rise to $\sim 50^{\circ}\text{C}$ could be measured when attaching a thermo element on the top surface of the beam. This temperature rise was believed to be the reason behind the drift in resonant frequency. A temperature rise of $\sim 30^{\circ}\text{C}$ should according to the analysis in [19] give a drop in stiffness of the foam of $\sim 10\%$. Setting adequate termination criterions for the test was not trivial given the large stiffness change caused by this change in temperature.

4 FE damping results

4.1 Modal analysis

Free-free

To initially validate the elastic properties and the geometry used as input in the FE model, a free-free modal analysis was performed in ANSYS[®]. The result from the analysis can be seen in Table 10. The correlation with the experimental results using the baseline material data is unsatisfactory, especially for the second and third mode, and is off with more than 5% which is regarded as limit for ok results at GAES[10]. There is an overestimation in stiffness for the first eigenmode whereas it at the same time is an underestimation for the second and third mode. This is an indication of that the bending stiffness may be overestimated while the shear stiffness is underestimated. One of the reasons for this was believed to be the deformation of the core and the resulting unsymmetric faces of the the test specimens described in Section 3.2. The effect of these geometrical defects on the stiffness was tested by a simplified modification of the FE-model where the thickness of the core was reduced to 6.5 mm and one of the faces was increased to 3 mm thickness. Since the thickness of the face was changed but the amount of fibre was kept constant, there had to be a change in fibre volume fraction. This change was input in the micromechanical model described in Section 2.2.3 which gave new elastic properties used as input to the elements in that face. The result from this modified model with unsymmetric faces can be seen in Table 10. It is clear that this modification only has a minor effect on the stiffness for the second and third mode. Based on this result it was assumed that the geometrical defects were not the reason for the discrepancy between experimental and numerical results.

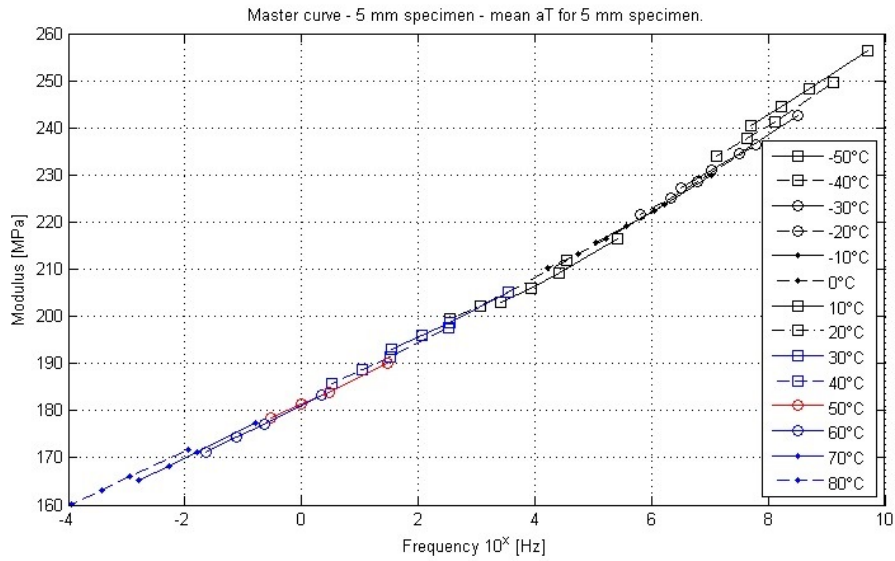
Table 10: Correlation in eigenfrequencies between experiment and FEA for free-free set-up.

Bending mode	1st [Hz]	Dev. [%]	2nd [Hz]	Dev. [%]	3rd [Hz]	Dev. [%]
Experimental	1355	–	2915	–	4501	–
Baseline	1415	+4.4	2610	–10.5	3982	–11.5
Unsymmetric faces	1384	+2.1	2605	–10.6	3995	–11.2
Stiffer core	1443	+6.5	2872	–4.6	4354	–3.3

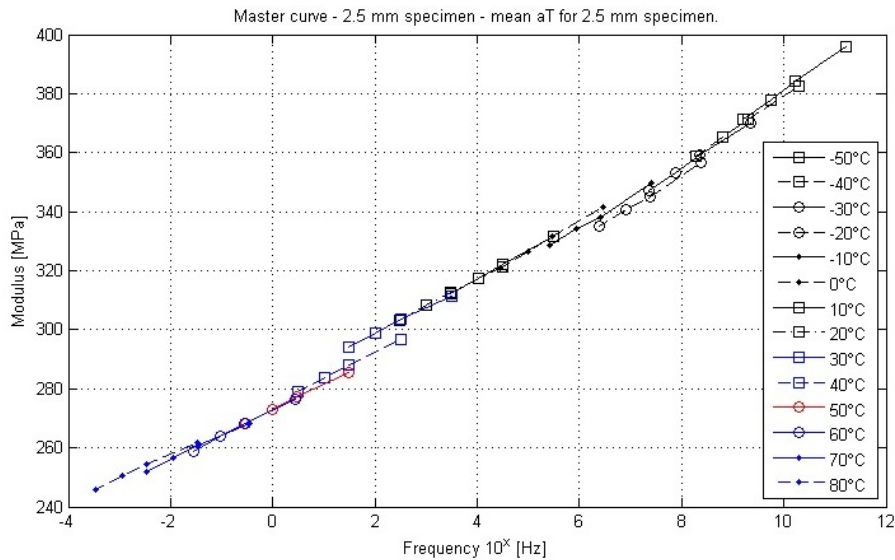
Another reason identified as a likely cause for the underestimation in shear stiffness was an incorrect input of the core stiffness. The preceding analyses up to this point was made using the static stiffness, 350 MPa, of the core stated by the manufacturer. The dynamic stiffness master curves from the DMTA performed on the foam material in [19] can be seen in Figures 50a and 50b. The absolute values of the modulus between the two test specimens differ and also show lower values than the static stiffness stated by the manufacturer. This means that the experimental data cannot be fully trusted and cannot be used in a quantitative sense. The frequency dependence of the modulus however is quite consistent between the two and shows a close to linear relation between modulus and frequency on the logarithmic scale for the frequency range of interest. The frequency and temperature span used in the DMTA was not wide enough to show any saturation of the modulus for lower frequencies which makes it difficult to set a reference as the static modulus in Figure 50. Using a rough estimate and assuming that the linear relation seen in the figures continues down to 10^{-6} Hz before saturating and reaching the static modulus one can expect an increase of the moduli of approximately 40% compared to the static value at the frequencies of the first bending modes. Therefore a new analysis was made with an increased stiffness to 500 MPa for the core. As seen in Table 10 this greatly improved the accuracy for the second and third bending mode while only slightly reducing the accuracy for the first mode. The overall improvement of the results with this modification shows that the frequency dependence of the core modulus has to be included in the analysis for accurate results. The constant value of 500 MPa is therefore used in all subsequent analyses.

Despite this modification a relatively large error remain given the rather simple geometry of the sandwich beam. However, considering the flaws in the geometry of the test pieces and there

unknown effect on mass and stiffness, together with the slight uncertain dynamic behaviour of the core material, the accuracy of the results are deemed acceptable.



(a) 5mm specimen



(b) 2.5mm specimen

Figure 50: *Dynamic modulus for the core material.*

Cantilever

The fixture used for the experimental cantilever ping test, seen in Figure 40b, should ideally correspond to a clamping of the beam to a base of infinite mass and stiffness. This is of course not true and a modal analysis with a 27.5 mm clamped length, as in the experimental test set-up, gives the frequencies seen in Table 11. Errors in frequency corresponding to the ones for the free-free condition in Table 10 should be expected. However the results are clearly stiffer than the experimental values and show that the real system deviates from the ideal cantilever case. For the most accurate results the stiffness of the bolt and washers should be included in the analysis. As a simplification the non-rigidity of the clamping mechanism was modelled as a reduction in

the clamped length. The eigenfrequencies for varying amount of clamping is seen in Table 11 and shows the sensitivity to the applied boundary condition. Apparently a clamped length of around 20 mm gives good correspondence with the experimental values when taking all three modes into account and will be used in subsequent analyses.

Table 11: Correlation in eigenfrequencies between experiment and FEA with different clamping length for cantilever set-up.

Bending mode	1st [Hz]	Dev. [%]	2nd [Hz]	Dev. [%]	3rd [Hz]	Dev. [%]
Experimental	241	–	1434	–	3408	–
27.5 mm	268	+11.2	1596	+11.3	3384	–0.7
20 mm	253	+5.0	1548	+7.9	3282	–3.7
15 mm	227	–5.8	1461	+1.9	3082	–9.6

4.2 Damping analysis

Harmonic analysis

Modelling the ping test technique used in the experimental testing explicitly in ANSYS[®] would require a transient dynamic analysis of an impulse load and the Fourier transform of the recorded time-history response. This technique would be extremely computationally expensive since the response would have to be computed with a sample rate corresponding to the frequency range of interest. A less computationally heavy solution is to instead perform a harmonic analysis where the frequency response to harmonic excitations is calculated and the damping is input in the analysis as described in Section 2.2.4. A drawback with this method is that a forced excitation has to be applied to the structure which means that a free-free condition cannot be simulated. Therefore, of the two ping tests performed in section 3.3.1 only the cantilever ping test can be simulated using this method. From the obtained frequency response curve in the harmonic analysis, the damping of each eigenmode can be calculated using the half-power method as described in Section 2.1.1. This method requires a high frequency resolution to capture the true shape of the response curve. With a too low resolution the damping will be overestimated since neither the eigenfrequency nor the half-power points will be found exactly. In this case the lowest eigenfrequency of interest is $f_0 \approx 250$ Hz where as low loss factors as $\eta \approx 1\%$ needs to be resolved, according to the results from the ping test in table 8. By rewriting Eq. (10) the necessary frequency resolution can be calculated to be at least

$$\frac{\Delta f}{2} = \frac{f_0 \eta}{2} = 1.25 \text{ Hz} \quad (42)$$

In turn, this mean that the response would have to be calculated ~ 3000 times to cover the entire frequency range of the three first bending modes. However, only the solutions near the eigenfrequencies are of interest since they are the ones used to calculate the damping of the modes. For the mode-superposition solving method, ANSYS[®] has a clustering option that clusters the solutions of the harmonic analysis around the eigenfrequencies found from an upstream modal analysis, reducing the required solutions while maintaining the resolution. For the regular full solution method however, the clustering option is not available since no upstream modal analysis is required in this method and the solver has no possibility to know at which frequencies the solutions should be clustered. To be able to use clustering in the full method, the clustering scheme for the mode-superposition method was implemented manually following the theory in [3].

The necessary harmonic excitation was introduced on the clamped end with a ± 1 mm displacement load in the vertical direction. The actual value of the excitation is not of importance and this value was simply chosen for easy normalisation. The response was measured at one of the nodes on the free end of the beam and the resulting response curve can be seen in Figure 51. Since the node chosen for measuring the response is located at the peak of the first mode shape, the response is higher for that mode than the other two. The implementation of the clustering scheme can clearly be seen by the higher density of solution points near the eigenfrequencies.

There is no guarantee that a solution point coincide exactly with the eigenfrequency or the

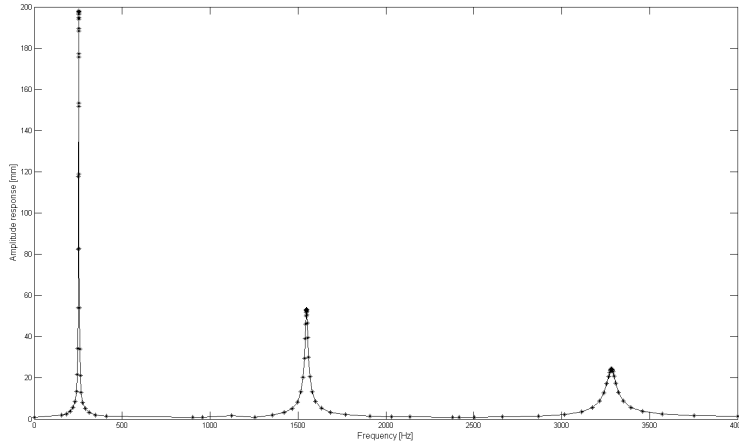


Figure 51: *Frequency response function for the cantilever set-up from a harmonic analysis in ANSYS® with clustered solutions.*

half-power points using this method, which means that some sort of curve fit or interpolation is needed to find these points. The curve fitting chosen is based on the analytical expression for the response of a SDOF damped mechanical system. The expression is given by

$$H = \frac{1/k}{\sqrt{\left(1 - \frac{\omega}{\omega_0}\right)^2 + \left(\frac{2\zeta\omega}{\omega_0}\right)^2}} \quad (43)$$

where k is the stiffness, ω_0 is the eigenfrequency and ζ is the damping ratio. The three parameters are found using a least-square-error method to create a best fit to the FEA response data.

Damped modal analysis

As mentioned earlier it is not possible to simulate the free-free ping test using the analysis method above. In the current case it is the modal damping of the beam which is of interest rather than the response curve. Fortunately there is a simpler method to calculate the modal damping in ANSYS® than through a harmonic analysis which can also be used for the free-free condition. When performing a so called damped modal analysis, the modal damping can simple be extracted at the end of the analysis. A damped modal analysis is performed by solving the equation of motion for a free system

$$-\omega^2 \mathbf{M}\mathbf{x} + i\omega \mathbf{C}\mathbf{x} + \mathbf{K}\mathbf{x} = \mathbf{0} \quad (44)$$

Since all eigenfrequencies and eigenmodes are found simultaneously using this equation it is not possible to construct the damping matrix as for the harmonic analysis, i.e., using the constant damping ratio, g_j , in Eq. (26). Instead, the damping matrix is constructed as [3]

$$[\mathbf{C}] = \alpha[\mathbf{M}] + \beta[\mathbf{K}] + \sum_{i=1}^{N_{ma}} \alpha_i^m [\mathbf{M}_i] + \sum_{j=1}^{N_{mb}} \beta_j^m [\mathbf{K}_j] \quad (45)$$

To create a constant damping matrix in the damped modal analysis on the same form as in the harmonic analysis, $\frac{g_j}{\omega_i}$, it is necessary to divide the stiffness matrix multiplier with the eigenfrequency, ω_i . To be able to do this one has to first perform an undamped modal analysis and find the eigenfrequencies of the system. It is then possible to construct the damping matrix by using the stiffness matrix multiplier, β_j^m , and scaling it with the found eigenfrequency, ω_i . The modal damping ratio for each mode can now be found by performing an individual damped modal analysis for each mode using its specific damping factor $\frac{\beta_j^m}{\omega_i}$.

4.3 Correlation between FE damping and experimental results

The predicted damping values found using harmonic analysis and damped modal analysis compared to the experimental results found in Section 3 for both free-free and cantilever set-up can be seen in Figures 52 and 53 and Tables 12 and 13.

To get an indication of the individual contribution from the core and CFRE to the total damping, an analysis was made where only the core damping was included. Given the slightly uncertain dynamic properties of the core an additional analysis was made with the core damping increased from 2.5% to 3.5%. The manufacturer of the resin material states a higher damping value than the one found through DMTA. Therefore an analysis was made using 10% resin damping instead of 4% to see which value gives the better correlation with the experimental data. From Section 2.2.6 it was found that the interphase between fibre and matrix could have a large influence on the total damping. Therefore an analysis was made simulating having a weak interphase by introducing an In-Plane (IP) longitudinal shear damping in the fibre of 1%. The effect of fibre damping, although in literature often stated to be negligible for carbon fibre, was tested by introducing an isotropic damping value of 0.5% in all fibre directions.

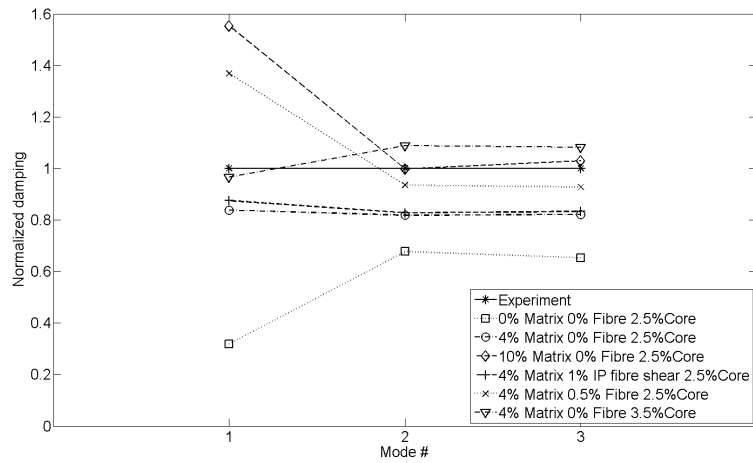


Figure 52: Correlation in damping, η , between experiment and FEA for free-free set-up.

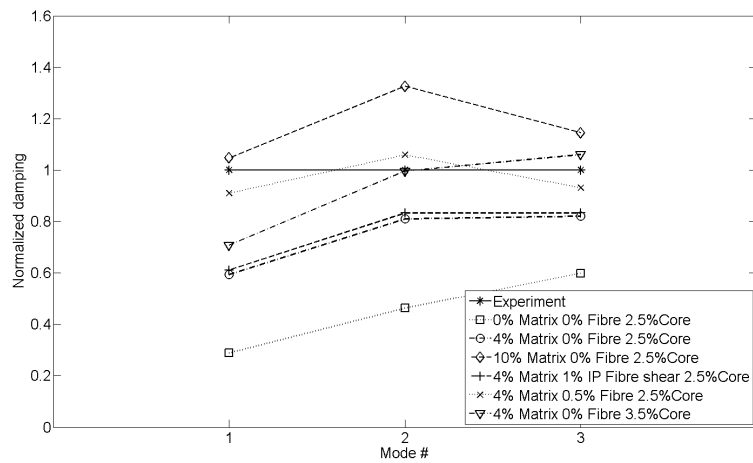


Figure 53: Correlation in damping, η , between experiment and FEA for cantilever set-up.

Table 12: Correlation in damping, η , between experiment and FEA for free-free set-up.

Bending mode	1st [Hz]	Dev. [%]	2nd [Hz]	Dev. [%]	3rd [Hz]	Dev. [%]
Experiment	0.76	–	1.85	–	1.94	–
Baseline	0.64	–15.8	1.51	–18.4	1.59	–18.0
0% matrix	0.24	–68.4	1.25	–32.4	1.27	–34.5
10% matrix	1.18	+55.3	1.85	± 0	2.00	+3.1
3.5% core	0.73	–3.9	2.01	+8.6	2.10	+8.2
1% IP fibre shear	0.67	–11.8	1.53	–17.3	1.62	–16.5
0.5% Isotropic fibre	1.04	+38.2	1.73	–6.5	1.80	–7.2

Table 13: Correlation in damping, η , between experiment and FEA for cantilever set-up.

Bending mode	1st [Hz]	Dev. [%]	2nd [Hz]	Dev. [%]	3rd [Hz]	Dev. [%]
Experiment	1.21	–	1.30	–	1.94	–
Baseline	0.72	–40.5	1.03	–21.8	1.59	–18.0
0% matrix	0.35	–71.1	0.60	–53.8	1.16	–38.9
10% matrix	1.27	+5.0	1.72	+32.3	2.22	+14.4
3.5% core	0.86	–28.9	1.29	+0.8	2.06	+6.2
1% IP fibre shear	0.74	–38.8	1.08	–16.9	1.62	–16.5
0.5% Isotropic fibre	1.10	–9.1	1.38	+6.2	1.81	–6.7

When comparing the damping results from the cantilever and free-free set-up it is clear that they share a similar trend for the second and third mode whereas there are some differences in the first mode where the FEA of the cantilever set-up gives a much larger underestimation of the experimental damping. The mode shapes in the two set-ups are similar and should therefore give similar damping. The high damping in the cantilever experimental results for the first mode is an indication that the fixture may have added a significant amount of extraneous damping. All conclusions made below are therefore made based on the results from the free-free set-up only.

Using the experimentally determined constituent material data is shown to give a clear underestimation of the damping for all modes. Looking at the results from the analysis with only core damping included it is clear that the composite has a decreasing contribution to the total damping for increasing modes, due to increasing amount of shear deformation in the core. Increasing the damping in the core to 3.5% gives overall damping closer to the experimental values but with a tendency to overestimation instead. This is an indication that the damping value of $\sim 2.5\%$ found in [19] is close to the actual value. By increasing the damping of the matrix to 10% an overestimation of the composite damping is experienced which gives a large error for the first mode. This means that the 4% value found from the DMTA is probably closer to the accurate value. Only a very small increase in damping is found when introducing damping in fibre shear which is most probably due to the relatively small amount of in-plane shear in this case with a 0° and 90° dominated lay-up and small bending-twisting coupling. This also shows that the behaviour of the CFRE more closely resembles that of the glass than the Kevlar[®] composite. Introducing 1% damping in the fibre gives the same type of overestimation of the composite damping as when increasing the matrix damping.

5 Conclusions

The method developed for prediction of the CFRE damping show promising results. The added effort compared to a regular dynamic FEA is that one additional material card has to be defined and that all elements has to be duplicated and equivalenced. The method requires twice the amount of elements which increases the computational cost when assembling the global stiffness and mass matrices. However once this is done the computational cost is the same since the number of DOF are kept constant. E.g., a 70% increase in number of elements was required in the analyses of the detailed sandwich beam specimen but only a 20% increase in solution time was experienced during a harmonic analysis.

The results from the damping analysis show that the CFRE has a large contribution to the damping in the sandwich structure, and especially for lower modes. This means that accurate modelling of the CFRE damping is needed when predicting the vibrational amplitudes in dynamic analyses.

Compared to a loss factor of $< 0.1\%$ for conventional metals like titanium and aluminium, the damping in the composite is significant and is a major design benefit when used in structural applications such as the OGV which experience large excitations.

The validation of the damping model in Section 2.2.6 showed that it is possible to predict the experimental results by adapting the different damping parameters in the model. However, in doing so the parameters may lose some of their physical meaning.

The underestimation of the structural damping when using the proposed method is believed to be caused mainly by the micromechanical model. Although most micromechanical models have been developed to predict the strength or stiffness properties of the composite they can also be used to, at least approximately, predict the damping properties. During derivation of the simplified micromechanical models some necessary assumptions of the material had to be made. E.g., that the composite is free of voids, that there is perfect bond between fibre and matrix, i.e. no interface region, and that the fibres are regularly spaced and aligned. These assumptions are of course not true for a real material but has proven to be reasonable when prediction the stiffness of the composite. These imperfections in the material might however have a greater impact on the damping properties of the material. There is therefore a risk of underestimating the damping in the composite using this approach since the actual causes of the internal damping in the material are not considered. This underestimation of the damping in turn means that the method is conservative in a HCF design point of view.

The viscoelastic behaviour of the foam core is clear with a significant temperature and frequency dependence which has to be included in a detailed analysis. For the matrix, and thereby the CFRE, however this behaviour is not as prominent. Although the frequency dependence of neither stiffness or damping has been included in the current thesis it can be introduced in ANSYS[®] using the command *MP,SDAMP*.

The damping in the CFRE is mostly matrix dependent. The damping values for neat resin, found from the DMTA, is much lower than the one stated from the manufacturer. Validation against experimental values for the sandwich beam indicates that the value from DMTA is the more accurate.

Only one damping factor can be assigned per element in ANSYS[®] and is decided by the material type assigned to the element as a whole. This will cause problem when using multiple-material elements, e.g., SOLSH190 or SOLID185, and trying to model multiple materials with different damping in a single element. This is not a problem when modelling composite layers of different orientations since the element still only consist of one type of material. However, this makes it impossible to model the damping of a complete sandwich structure using only one element through the thickness.

By looking at Tables 12 and 13 it is clear that the modal damping is different for each mode. This means that it is not sufficient to include damping by simply assigning a constant modal damping ratio in a mode-superposition harmonic analysis. Instead, the damping ratio has to be identified for each mode separately using a damped modal analysis and then input to the analysis. This is not an issue when performing a full harmonic analysis since it in that case is possible to define a constant structural damping ratio for the material.

6 Future work

Initial HCF testing showed that it was possible to initiate fatigue failure in the core for at least 10^6 cycles using the developed design. Further work is needed in setting the parameters and excitation levels for the HCF test series. Only then is it possible to say if the test set-up is capable of testing the HCF capability of the core up to 10^8 cycles. The procedure for the continued HCF testing is covered in [17].

With the current computer set-up for the HCF test it is only possible to observe the immediate response from the test specimen. In the continued work recording of the signals should be considered for easier observation of the fatigue process and identification of crack initiation and propagation.

The test specimens used have a slightly deformed core with unknown effects on stiffness, damping and fatigue properties. For a real HCF verification test new test specimens have to be made with minimum amount of defects.

Temperature measurement on the top surface of the sandwich beam was made in this initial stage of the HCF testing and showed a significant temperature build-up in the specimen. Work should be focused on measuring the actual temperature of the core and CFRE to determine its effect on stiffness and the HCF capability. The temperature build up should also be related to the in-service intermittent excitations experienced by the OGV.

During the relatively aggressive excitation during the initial HCF test there was some indication that the amplitude response did not change linearly with change in excitation amplitude. This means that the CFRE may exhibit nonlinear damping at the stress level needed for fatigue and it is suggested that more thorough tests are made at a range of stress amplitudes to clarify this behaviour.

There is a large scatter in the DMTA data for the foam core. It is recommended that a new DMTA test is made for increased confidence in the material data.

Only the Halpin-Tsai micromechanical damping model has been investigated. Not much difference between the different micromechanical models presented in [27] can be seen. However, it would be interesting to see if a different choice of micromechanical model can give a better prediction of the CFRE damping.

The FE modelling technique used through this thesis is based on FSDT which underpredicts the damping for thick laminates due to its inability to capture interlaminar effects. Continued work should be focused on the implementation of a HSDT FE-model and evaluation of its need for accurate damping predictions.

Only the material damping in the composite sandwich has been covered in this thesis. The combined damping from both internal damping and extraneous sources in a real application has to be considered when performing HCF estimation.

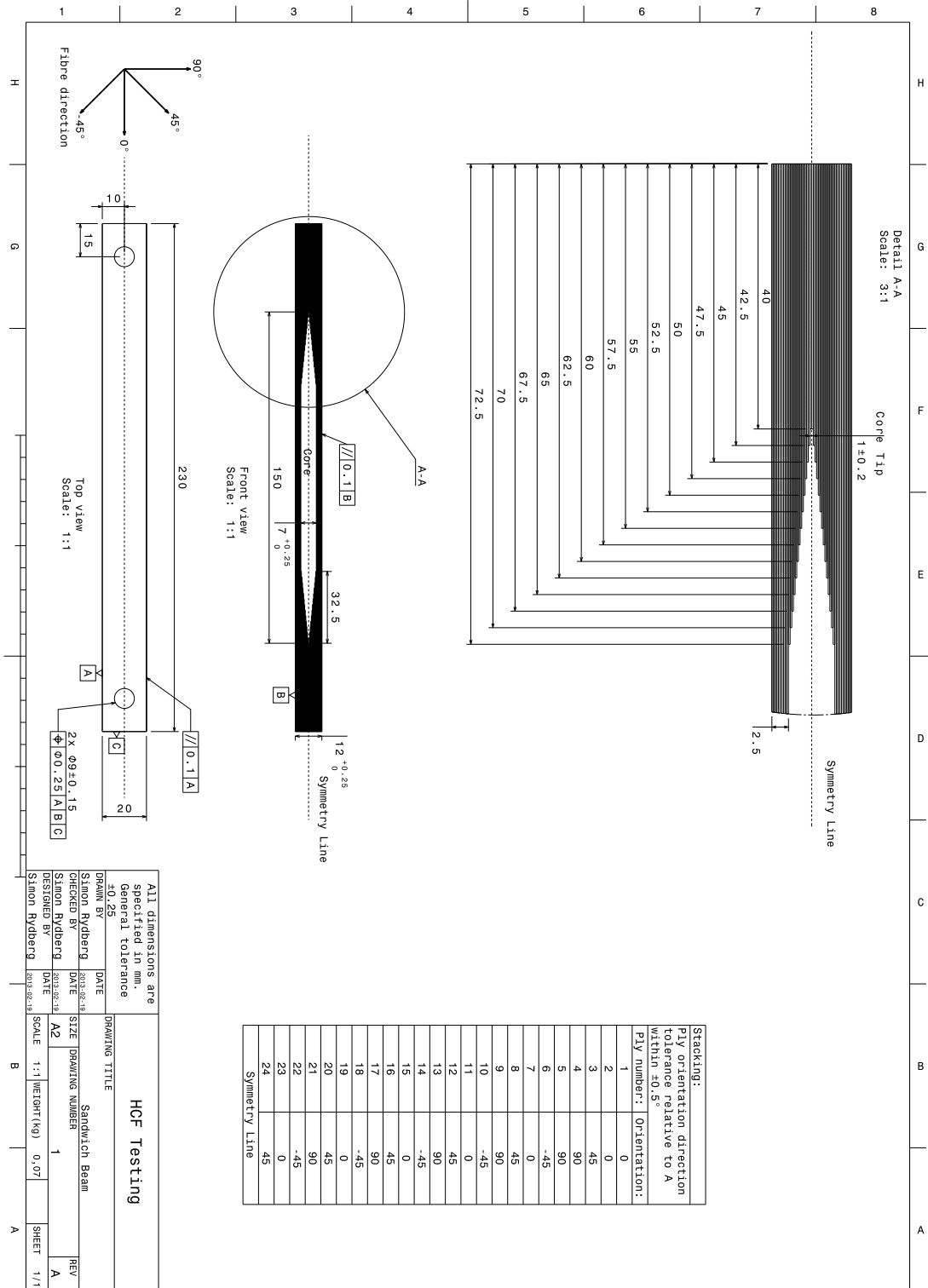
There are many unknowns regarding the exact damping mechanisms on a micromechanical level. As for the elastic properties of the CFRE which have been determined experimentally on a ply level, it is recommended that the same should be done for the damping properties. By doing this any errors in the predicted damping originating from the limitations of the micromechanical model can be avoided.

References

- [1] R. Adams. “The dynamic longitudinal shear modulus and damping of carbon fibres”. In: *Journal of Physics* 8 (1975), pp. 738–748.
- [2] *ANSYS Mechanical APDL Material Reference*. Version 14.0. ANSYS, Inc., 2011. URL: <http://www.ansys.com>.
- [3] *ANSYS Mechanical APDL Theory Reference*. Version 14.0. ANSYS, Inc., 2011. URL: <http://www.ansys.com>.
- [4] B. Åström. *Manufacturing of Polymer Composites*. Chapman & Hall, 1997. ISBN: 978-0748770762.
- [5] J.-M. Berthelot and Y. Sefrani. “Damping analysis of unidirectional glass and Kevlar fibre composites”. In: *Composites Science and Technology* 64 (2004), pp. 1261–1278.
- [6] R. M. Christensen. *Mechanics of Composite Materials*. John Wiley & Sons, 1979. ISBN: 0-471-05167-5.
- [7] *CR11-106 Strength testing of neat resin and NCF bundles under uniaxial and mixed in-plane loading*. Refact.
- [8] R. M. Crane and J. John W. Gillespie. “Analytical Model for Prediction of the Damping Loss Factor of Composite Materials”. In: *Polymer Composites* 13 (1995), pp. 179–190.
- [9] *Delivery programme and characteristics for filament yarn*. Toho Tenax Europe GmbH, 2011. URL: <http://www.tohotenax-eu.com>.
- [10] *Discussion with Anders Lindblom, Test Engineer at GAES*.
- [11] R. F. Gibson. *Principles of composite material mechanics*. McGraw-Hill, 1994. ISBN: 0-07-023451-5.
- [12] J. C. Halpin. *Primer on Composite Materials: Analysis*. Technomic, 1984. ISBN: 87762-349-X.
- [13] S. Hwang and R. Gibson. “Prediction of Fiber-Matrix Interphase Effects on Damping of Composites Using a Micromechanical Strain Energy/Finite Element Approach”. In: *Composites Engineering* 3 (1993), pp. 975–984.
- [14] S. Hwang and R. Gibson. “The Effects of Three-Dimensional States of Stress on Damping of Laminated Composites”. In: *Composites Science and Technology* 41 (1991), pp. 379–393.
- [15] D. I. G. Jones. *Handbook of Viscoelastic Vibration Damping*. John Wiley & Sons, 2001. ISBN: 0-471-49248-5.
- [16] R. M. Jones. *Mechanics of Composite Materials Second Edition*. Taylor & Francis, 1999. ISBN: 1-56032-712-X.
- [17] J. Juul. *VOLS:10184644, Test request for HCF test of composite sandwich beam with foam core*. 2013.
- [18] K.-N. Koo and I. Lee. “A refined Analysis of Vibration and Damping for Anisotropic Laminates in Cylindrical bending”. In: *Journal of Sound and Vibration* 184 (1995), pp. 553–566.
- [19] J. Langer. *Investigation and Simulation of the Heating Effects in Sandwich Cores During Vibrational Loading*. KTH, 2012.
- [20] B. J. Lazan. *Damping of materials and members in structural mechanics*. Pergamon Press, 1968.
- [21] G. A. Lesieutre. “On the Consistency of Complex Modulus for Transversely-Isotropic Viscoelastic Materials”. In: *Journal of Composite Materials* 28 (1994), pp. 382–391.
- [22] M. Lundgren. *Finite Element Analysis of a Composite Outlet Guide Vane With a Core*. KTH, 2008.

- [23] R. D. A. M. R. Maheri and J. Hugon. “Vibration damping in sandwich panels”. In: *Journal of Material Science* 43 (2008), pp. 6604–6618.
- [24] D. P. Makecha, M. Ganapathi, and B. P. Patel. “Vibration and Damping Analysis of Laminated/Sandwich Composite Plates Using Higher-Order Theory”. In: *Journal of Reinforced Plastics and Composites* 21 (2002), pp. 559–575.
- [25] *Product Data*. Hexcel, 2009. URL: <http://www.hexcel.com/resources/datasheets>.
- [26] R.Chandra, S. Singh, and K. Gupta. “Damping studies in fiber-reinforced composites - a review”. In: *Composite Structures* 46 (1999), pp. 41–51.
- [27] R.Chandra, S. Singh, and K. Gupta. “Micromechanical damping models for fiber-reinforced composites: a comparative study”. In: *Composites Part A* 33 (2002), pp. 787–796.
- [28] R. Reimers. *VOLS:10075986, Finite Element Pre-Requisites for Composite Modeling rev. 02*. 2010.
- [29] *ROHACELL. Product information*. Evonik Industries AG, 2013. URL: <http://www.rohacell.com>.
- [30] *Rohacell: The Core for Sandwich Solutions*. Evonik Industries AG, 2006.
- [31] R. F. G. S. J. Hwang and J. Singh. “Decomposition of Coupling effects on damping of laminated composites under flexural vibration”. In: *Composites Science and Technology* 43 (1992), pp. 159–169.
- [32] *VOLS:10171207, Development of a fatigue model for carbon fiber composites*. 2013.
- [33] D. Zenkert. *An Introduction to Sandwich Structures Second Edition*. Universitetservice, 2005.

A Manufacturing specification of sandwich beam specimen



B Exploded view of fixture assembly

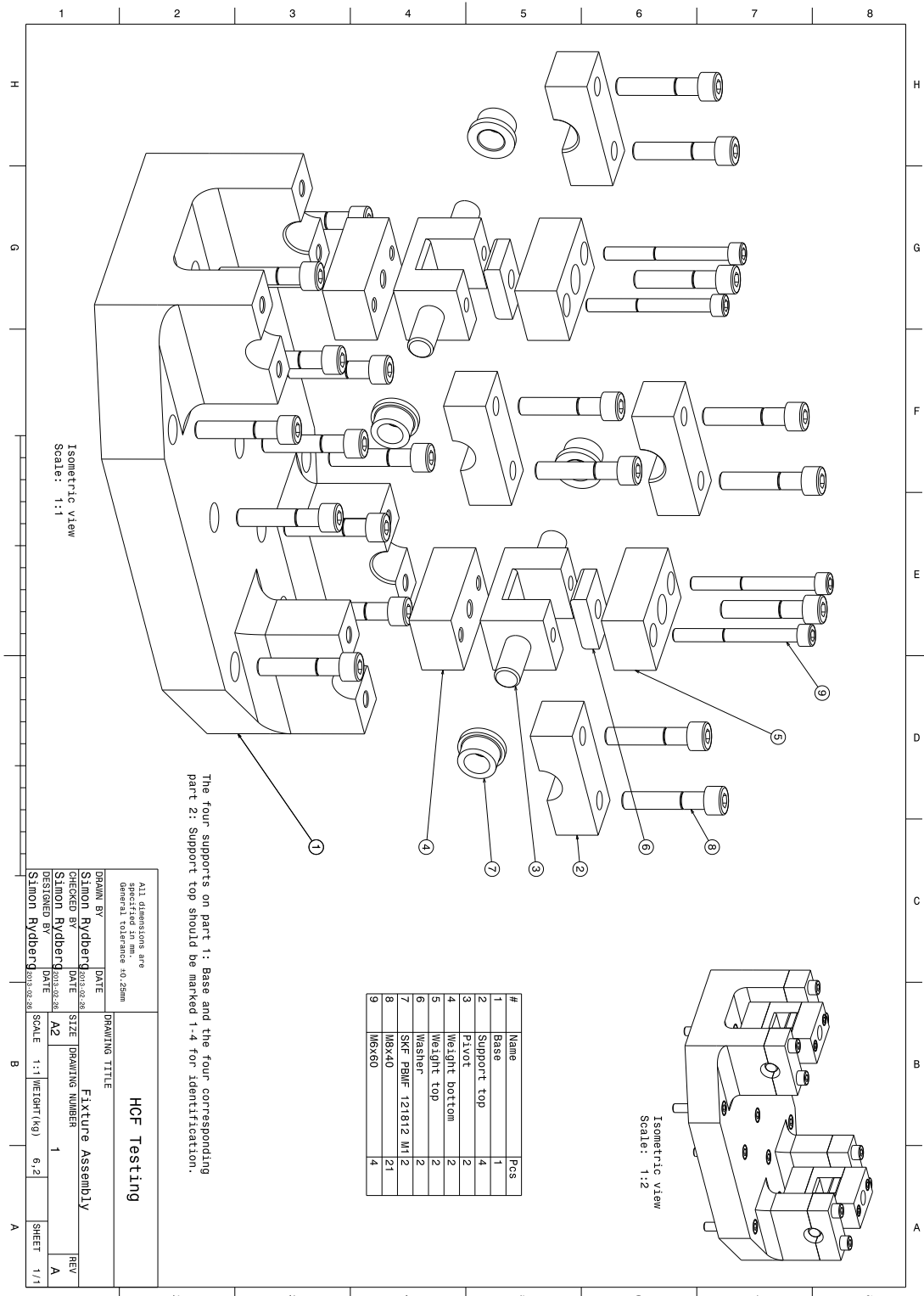


Figure 55: Exploded view of fixture assembly

C Modal analysis of fixture

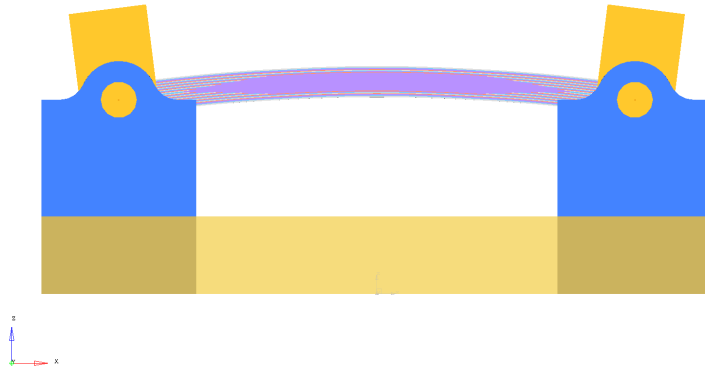


Figure 56: *First eigenmode of fixture and test specimen assembly.*

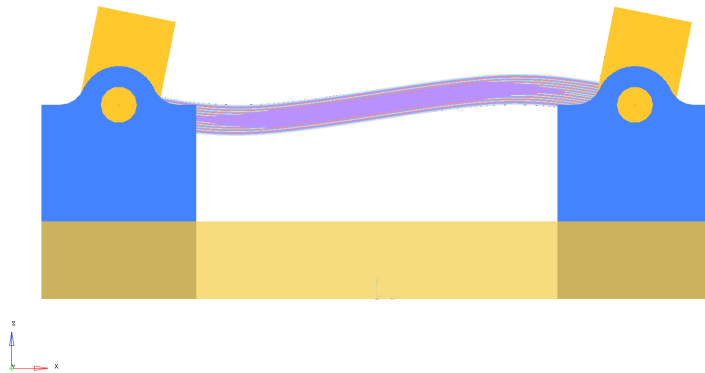


Figure 57: *Second eigenmode of fixture and test specimen assembly.*

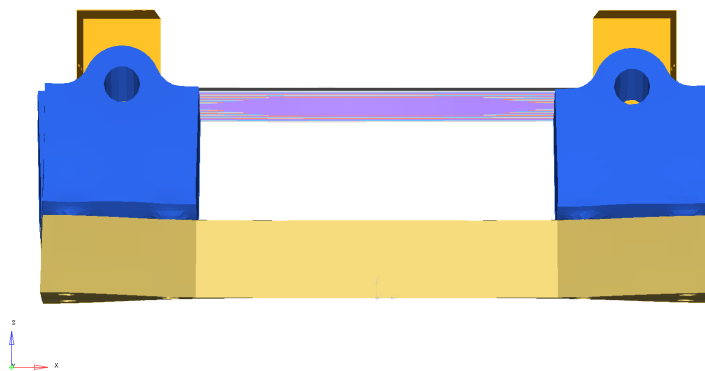


Figure 58: *Third eigenmode of fixture and test specimen assembly.*

D Matlab code

```
1 clear all
2 close all
3 clc
4 %%
5 %Matrix data
6 Em=5e3;
7 prm=0.3;
8 Gm=Em/(2*(1+prm));
9
10 %Composite data
11 E1=150e3;
12 E2=5e3;
13 prxy=0.5; %Exakt som rule of mixtures
14 pryz=0.5;
15 G12=5e3;
16 G23=E2/(2*(1+pryz));
17 Vf=0.6;
18
19 %From Halpin-Tsai, Primer on Composite Materials: Analysis p.130-136
20
21 %% Fibre longitudinal stiffness
22 Ef=(E1-(1-Vf)*Em)/Vf;
23
24 %% Fibre transverse stiffness
25 xsi=2;
26 eta=(E2/Em-1)/(Vf*(E2/Em+xsi));
27 E2_f_HT=Em*(1+xsi*eta)/(1-eta);
28
29 %% Fibre in-plane shear stiffness
30 xsi=1;
31 eta=(G12/Gm-1)/(Vf*(G12/Gm+xsi));
32 G12_f_HT=Gm*(1+xsi*eta)/(1-eta);
33
34 %% Fibre in-plane Poisson's ratio
35 prxy_f=(prxy-prm*(1-Vf))/Vf;
36
37 %% Fibre out-of-plane Poisson's ratio
38 xsi=2;
39 eta=(pryz/prm-1)/(Vf*(pryz/prm+xsi));
40 pryz_f_HT=prm*(1+xsi*eta)/(1-eta);
41
42 %% Fibre transverse shear stiffness
43 G23_f=E2_f_HT/(2*(1+pryz_f_HT));
44
45 %% Complex matrix data
46 tan_Δ=0.04;
47 Em2=Em*(1+tan_Δ*1i);
48 Gm2=Gm2/(2*(1+prm));
49
50 %% Complex composite longitudinal stiffness
51 E1_c=Ef*Vf+(1-Vf)*Em2;
52
53 %% Complex composite transverse stiffness
54 xsi=2;
55 eta=(E2_f_HT/Em2-1)/(E2_f_HT/Em2+xsi);
56 E2_c_HT=Em2*(1+xsi*eta*Vf)/(1-Vf*eta);
57
58 %% Complex composite in-plane shear
59 xsi=1;
60 eta=(G12_f_HT/Gm2-1)/(G12_f_HT/Gm2+xsi);
61 G12_c_HT=Gm2*(1+xsi*eta*Vf)/(1-Vf*eta);
62
63 %% Complex composite in-plane Poisson's ratio
64 prxy_c=prxy_f*Vf+prm*(1-Vf); %Will not be complex since assumed real
65
```

```

66 %% Complex composite out-of-plane Poissons's ratio
67 xsi=2;
68 eta=(pryz_f_HT/prm-1)/(pryz_f_HT/prm+xsi);
69 pryz_c_HT=prm*(1+xsi*eta*Vf)/(1-eta*Vf); %Will not be complex since assumed real
70
71 %% Complex composite transverse shear stiffness
72 G23_c=E2_c_HT/(2*(1+pryz_c_HT));
73
74 %% Complex Composite Tensor (TRANSVERSELY ISOTROPIC)
75 S=[ 1/E1_c -prxy_c/E1_c -prxy_c/E1_c 0 0 0;...
76     -prxy_c/E1_c 1/E2_c_HT -pryz_c_HT/E2_c_HT 0 0 0;...
77     -prxy_c/E1_c -pryz_c_HT/E2_c_HT 1/E2_c_HT 0 0 0;...
78     0 0 0 1/G23_c 0 0;...
79     0 0 0 0 1/G12_c_HT 0;...
80     0 0 0 0 0 1/G12_c_HT];
81
82 C=inv(S);
83
84 S_storage=inv(real(C));
85 S_loss=inv(imag(C));
86
87 %% Input for storage moduli element
88 E1_storage=1/S_storage(1,1);
89 E2_storage=1/S_storage(2,2);
90 E3_storage=E2_storage;
91 G12_storage=1/S_storage(6,6);
92 G13_storage=G12_storage;
93 G23_storage=1/S_storage(4,4);
94 prxy_storage=-S_storage(1,2)/S_storage(1,1);
95 prxz_storage=prxy_storage;
96 pryz_storage=-S_storage(2,3)/S_storage(2,2);
97
98 %% Input for loss moduli element
99 E1_loss=1/S_loss(1,1);
100 E2_loss=1/S_loss(2,2);
101 E3_loss=E2_loss;
102 G12_loss=1/S_loss(6,6);
103 G13_loss=G12_loss;
104 G23_loss=1/S_loss(4,4);
105 prxy_loss=-S_loss(1,2)/S_loss(1,1);
106 prxz_loss=prxy_loss;
107 pryz_loss=-S_loss(2,3)/S_loss(2,2);

```